TÉCNICO LISBOA

# Scalar Fields, Black Holes and Spherical Coordinates

**Gonçalo João Correia de Andrade**

Thesis to obtain the Master of Science Degree in

## Engineering Physics

Supervisor(s): Dr. Miguel Rodrigues Zilhão Nogueira

### Examination Committee

Chairperson: Prof. José Pizarro de Sande e Lemos
Supervisor: Dr. Miguel Rodrigues Zilhão Nogueira
Member of the Committee: Prof. David Mathew Hilditch

**January 2021**

To my parents.

# Acknowledgments

Working on this project for the past few months was, without a doubt, the most challenging experience of my life. Yet, it was also extremely enjoyable, and it made me realise that physics is what I want to work on for the rest of my life. However, I did not do it alone. There were several people that helped me get through the hardships that came along with the writing of this thesis, and I would like to express my appreciation for those people.

First, and foremost, my supervisor Miguel. We met for the first time when he thought an introductory course on Numerical Relativity and in which I was enrolled. Immediately I decided that I'd like to work on this field for my thesis, as it put together both of my favourite areas in physics: General Relativity and computational physics. The rest, as they say, is history. Miguel has helped me with understanding the core foundations of Numerical Relativity, through all the bugs and uncertainties that emerged from a numerical implementation of this magnitude on a code none of us knew, and through the analysis of our results. Throughout this thesis, I consistently refer to it as "our" work, and not mine, because none of it would be possible without Miguel. For that, thank you.

I like to extend my thanks to CENTRA and GRIT, for allowing me to be included in group meetings and seminars, and for providing the computational resources I needed to obtain the results I did. Furthermore, I would also like to thank Prof. Zachariah Etienne at West Virginia University, the lead of development of NRPy+, for his valuable contributions and discussions towards a successful implementation of our code within this tool.

Last, but certainly not least, I must thank my girlfriend, Mariana, and my parents. They have been with me through the whole duration of my stay at Instituto Superior Técnico (even before that, in the case of my parents), they have supported me through every difficult decision I had to make, through every difficulty and every achievement, and I owe them everything. If it wasn't for their support, I would probably not be here today. Thank you, for everything.

# Resumo

Buracos negros são dos objetos mais simples previstos pela Relatividade Geral. No entanto, são responsáveis por uma quantidade de fenómenos interessantes nas suas vizinhanças. Entre estes está a interação de campos de matéria com a geometria, através de oscilações quasi-normais e emissão de ondas gravitacionais. O estudo destes fenómenos pode fornecer informação relevante para a procura de matéria escura através de astronomia de ondas gravitacionais ou outras fontes de dados astrofísicos.

Nesta tese explora-se a interação de campos escalares reais, descritos pela equação de Klein-Gordon, em espaços-tempo de buraco negro. A nossa abordagem foca-se no uso de coordenadas esféricas para tirar partido das simetrias aproximadas do problema. Para isso, começamos por introduzir o formalismo da Relatividade Numérica e a formulação BSSN, bem como algumas técnicas que permitem o uso de sistemas de coordenadas curvas genéricos. Seguidamente, fazemos uso dessas técnicas para evoluir as quantidades métricas e as variáveis de matéria de forma não-linear. Foram implementados, na ferramenta de geração de código NRPy+, módulos que permitem a evolução de campos escalares, minimamente acoplados à gravidade. Os nossos resultados para a interação não-linear de campos sem massa, bem como a evolução de estados pseudo-ligados de campos massivos, são coerentes com estudos lineares e não-lineares existentes na literatura.

**Palavras-chave:** Relatividade Numérica, Coordenadas Esféricas, Campos Escalares, Buracos Negros, Matéria Escura, Relatividade Geral

## Abstract

Black holes are some of the simplest objects predicted by General Relativity, yet they give rise to a number of interesting phenomena in their vicinities. Amongst these is the interaction of matter fields with the geometry, through quasi-normal oscillations and gravitational wave emission. Studying such phenomena could provide valuable insights towards dark matter searches from gravitational wave astronomy and other sources of astrophysical data.

In this thesis we explore the scattering of real scalar fields, described by the Klein-Gordon equation, with black hole spacetimes. Our approach focuses on the use of spherical coordinates to take advantage of the approximate symmetries of the problem. To do so, we start by introducing the formalism of Numerical Relativity and the BSSN formulation, along with techniques that allow the use of general curvilinear coordinate systems. Then, we make use of those techniques to evolve both the metric quantities and matter variables in a non-linear fashion. We implemented, within the code generation tool NRPy+, modules that allow for the evolution of scalar fields minimally coupled to gravity. Our results for the non-linear scattering of massless fields, as well as the evolution of pseudo-bound states of massive fields, are consistent with previous linear and non-linear studies in the literature.



**Keywords:** Numerical Relativity, Spherical Coordinates, Scalar Fields, Black Holes, Dark Matter, General Relativity

# Contents

# List of Tables

# List of Figures

# Nomenclature

### Greek symbols

| | |
|---|---|
| $\alpha$ | Lapse function |
| $\bar{\Lambda}^a$ | Evolving quantity in the covariant BSSN formalism built from $\Delta^a$ |
| $\beta^a$ | Shift vector |
| $\Delta^a_{bc}$ | Difference between Christoffel symbols of the conformal and reference metrics |
| $\delta_{ab}$ | Kronecker delta |
| $\Gamma^a_{bc}$ | Christoffel symbols |
| $\gamma_{ab}$ | 3-dimensional spatial metric tensor |
| $\lambda^a$ | Rescaled variant of $\bar{\Lambda}^a$ |
| $\mu_S$ | Mass coupling for a Klein-Gordon field |
| $\nabla$ | Covariant derivative compatible with the 4-dimensional metric $g$ |
| $\omega$ | Frequency |
| $\phi$ | Alternative conformal factor used in BSSN |
| $\Phi, \Pi$ | Scalar field variables |
| $\psi$ | Conformal factor |
| $\Psi_4$ | Weyl scalar related to outgoing gravitational waves |
| $\rho$ | Energy density measured by a normal observer |
| $\Sigma_t$ | Spacelike 3-dimensional hypersurface of constant coordinate time $t$ |
| $\theta, \varphi$ | Spherical angular coordinates |
| $\varepsilon_{ab}$ | Difference between the conformal and reference spatial metric tensors |

### Roman symbols

| | |
|---|---|
| $\chi$ | Black hole dimensionless spin |

| | |
|---|---|
| $\mathcal{B}^a$ | Rescaled variant of $B^a$ |
| $\mathcal{H}$ | Hamiltonian constraint violation |
| $\mathcal{L}$ | Lie derivative |
| $\mathcal{M}$ | Spacetime manifold |
| $\mathcal{M}^a$ | Violation of the component $a$ of the momentum constraints |
| $\mathcal{V}^a$ | Rescaled variant of $\beta^a$ |
| $\mathrm{d}l^2$ | 3-dimensional line element |
| $\mathrm{d}s^2$ | 4-dimensional line element |
| $\mathtt{x}i$ | NRPy+ numerical grid coordinate in the direction of $x^i$ |
| $\partial_a$ | Partial derivative with respect to coordinate $x^a$ |
| ${}_sY_{lm}$ | Spin-weighted spherical harmonics |
| $a$ | Black hole spin per unit mass |
| $A_P$ | Amplitude for the initial data of pseudo-bound type for the scalar fields |
| $A_{00}$ | Amplitude for the initial data of Gaussian type for the scalar fields |
| $A_{11}$ | Amplitude for the initial data of dipolar type for the scalar fields |
| $A_{ab}$ | Traceless part of the extrinsic curvature |
| $a_{ab}$ | Rescaled variant of $A_{ab}$ |
| $B^a$ | Auxiliary variable for hyperbolic gamma driver shift evolution |
| $D$ | Covariant derivative compatible with the 3-dimensional metric $\gamma$ |
| $g_{ab}$ | 4-dimensional metric tensor |
| $h_{ab}$ | Rescaled variant of $\varepsilon_{ab}$ |
| $K$ | Trace of the extrinsic curvature |
| $K_{ab}$ | Extrinsic curvature |
| $M$ | Black hole mass |
| $n^a$ | Future directed unit vector normal to $\Sigma_t$ |
| $N_{\mathsf{FD}}$ | Order of accuracy of finite difference operators |
| $N_{\mathsf{G}}$ | Number of ghost points in a numerical grid |
| $N_a$ | Number of grid points along the direction $x^a$ |

$Q$ Black hole electric charge

$R$ Ricci scalar

$r$ Spherical radial coordinates

$r_0, w$ Gaussian centre and width for scalar fields initial data

$R_{\text{max}}$ Maximum value for the radial coordinate

$r_h$ Event horizon radius

$R_{abcd}$ Riemman curvature tensor

$R_{ab}$ Ricci tensor

$S$ Trace of the spatial stress tensor

$S_a$ Momentum density measured by a normal observer

$S_{ab}$ Spatial stress tensor

$t$ Time coordinate

$T_{ab}$ 4-dimensional stress-energy tensor

$w_s$ Scaling parameter for *SinhSpherical* coordinates

$x, y, z$ Cartesian coordinates

$x^a$ General designation for a coordinate function in any coordinate system

**Subscripts**

$(ij)$ Symmetrisation of a tensor on indices $ij$

$[ij]$ Anti-symmetrisation of a tensor on indices $ij$

$\mu, \nu, ...$ Spacetime tensor components (also used as superscript)

$a, b, c...$ Tensor indices in abstract index notation (also used as superscript)

$i, j, k...$ Spatial tensor components (also used as superscript)

$s, l, m$ Quantum numbers for spin-weighted spherical harmonics

QNM Refering to the quasi-normal modes of oscillation

**Superscripts**

$\bar{}$ Conformally related quatity

$\hat{}$ Quantity related to the reference metric

$(4)$ 4-dimensional quantity

| | |
|---|---|
| * | Complex conjugate |
| TF | Trace-free part of a tensor |

# Glossary

| | |
|---|---|
| **ADM** | Arnowitt, Deser and Misner, usually refers to the Hamiltonian formulation of General Relativity proposed by these authors |
| **AdS/CFT** | Anti-de Sitter / Conformal Field Theory correspondence, a duality between gravity in Anti-de Sitter spacetimes and a class of Quantum Field Theories |
| **BSSN** | Baumgarte-Shapiro-Shibata-Nakamura formulation of the 3+1 decomposition of Einstein's equations |
| **C** | A programming language |
| **LIGO** | Laser Interferometer Gravitational-Wave Observatory |
| **MoL** | Method of Lines |
| **NRPy+** | A Python infrastructure for generating C code for Numerical Relativity simulations |
| **ODE** | Ordinary differential equation |
| **PDE** | Partial differential equation |
| **Python** | A programming language |
| **QNM** | Quasi-Normal Mode |
| **QPE** | Quadratic Polynomial Extrapolation, a type of outer boundary conditions implemented within NRPy+ |
| **RK4** | Fourth order Runge-Kutta method |
| **SymPy** | A Python library for symbolic calculation |
| **TOV** | Tolman–Oppenheimer–Volkoff, usually refers to an equation that describes a spherically symmetric star in gravitational equilibrium |
| **Wolfram Mathematica** | A software used for symbolic computations and data analysis, amongst other things |

# Chapter 1

# Introduction

## 1.1 Motivation & Overview

Gravity, from the Latin *gravitas*, meaning "weight", is one of the four fundamental interactions in physics. It is the process through which all objects in the universe are attracted towards each other. It is responsible for several everyday phenomena, like the falling of objects or the tides of the oceans, as well as large scale processes in the universe, such as the formation of galaxies, and even some exotic occurrences, like black holes (more on that later).

Ever since humans started thinking rationally about the world around them, it was clear that gravity played a central role in the universe. However, it was with the Scientific Revolution, starting in the late 16th century, that major theoretical achievements started to appear. It was during this time that Galileo showed, through the famous experiment performed in the Leaning Tower of Pisa, that the gravitational acceleration at Earth's surface is independent of the object experiencing it. Not long after came Isaac Newton, who proposed the first proper theory of gravity. In this theory, the gravitational force $F_g$ experienced by an point mass $m_1$ due to another mass $m_2$ is given by

$$F_g = \frac{Gm_1m_2}{r^2}, \tag{1.1}$$

where $r$ is the distance between the two masses, and $G$ is the universal gravitational constant. Through Newton's second law, one can obtain the equations of motion for bodies subjected to $F_g$. Newton's theory, frequently referred to as *Newton's Law of Universal Gravitation*, had its share of successes over the years. Its first test was the Cavendish experiment, in 1798, which led to an accurate measurement of $G$. Almost a century later, the theory was used by John Couch Adams and Urbain Le Verrier to predict the existence of Neptune, which was later discovered by Johann Gottfried Galle, by noticing that the orbit of Uranus was not consistent with the current catalogue of planets. However, there were things the theory was not able to explain, the most well-known being the precession of Mercury's perihelion.

In 1905, Albert Einstein noted, in one of his seminal papers, that there were inconsistencies between Maxwell's theory of electromagnetism and the notion of absolute motion present in Newtonian mechan-

ics. Indeed, Einstein pointed out that, in electromagnetism, observable phenomena depended only on the relative motion of bodies. This point, together with the fact that no evidence of the *luminiferous ether* – a medium which was thought to be responsible for the propagation of light, and according to which absolute movement could be defined – had been found, led Einstein to formulate the *Principle of Relativity*: "for all coordinate systems for which the mechanical equations hold, the equivalent electrodynamical and optical equations hold also" [1], *i.e.* the laws of physics are invariant in all inertial frames of reference. This principle, together with the postulate that light propagates with a definite velocity $c$, regardless of the frame of reference considered, led to the proposal of *Special Relativity*. From this theory stemmed rather jarring consequences, like length contraction and time dilation. Space and time were no longer separate entities, but rather one unique reality: *spacetime*.

Although groundbreaking, Special Relativity only tells us to use Lorentz transformations (instead of Galilean transformations) when moving from one inertial frame to another. This means that it is not valid, for example, in a frame with non-negligible gravitational effects. However, it did inspire Einstein to expand it to include gravity. This was accomplished in 1915, with the publication of a series of papers where a new geometric theory of gravitation was established, which was suitably named *General Relativity*. In opposition with Newton's Law of Universal Gravitation, General Relativity does not treat gravity as a force, but rather as a geometric effect. Indeed, spacetime is now seen as a dynamic continuum, which may have a flat or a curved geometry. The geometry of spacetime is encoded in the metric tensor $g_{ab}$, which obeys Einstein's field equations,

$$R_{ab} - \frac{1}{2} R \, g_{ab} = 8\pi \, T_{ab}, \tag{1.2}$$

where $R_{ab}$ and $R = g_{ab}R^{ab}$ are the *Ricci tensor* and the *Ricci scalar*, respectively, and $T_{ab}$ is the *stress-energy tensor*. The left-hand side of Eq. (1.2) is built from the Riemann tensor, so it is associated with the curvature of the metric. The stress-energy tensor, on the right-hand side, is related to the density of mass-energy in the universe, and it acts as a source of curvature (and gravity). In the manifold that is spacetime, point particles to which no force is applied follow a class of trajectories called *geodesics*. In the flat spacetime of Special Relativity, the geodesics equate to a straight line trajectory, hence validating Newton's law of inertia in this regime. However, when the metric is non-trivial (not flat), geodesics deviate from the previous case due to the curvature, resulting in the gravitational effects we see throughout the universe.

Having the field equations (1.2), one now intends to solve them, in order to obtain physically meaningful solutions. This is no easy task – although the equations look simple, they are actually a set of ten coupled non-linear partial differential equations containing hundreds, if not thousands of terms when fully expanded. Nevertheless, some analytic solutions have been found. The first one was discovered by Schwarzschild in 1916 [2], just one year after the publication of the field equations. This solution

describes a spherically symmetric geometry, and its line element $\mathrm{d}s^2 = g_{ab}\mathrm{d}x^a\mathrm{d}x^b$ is given by

$$\mathrm{d}s^2 = -\left(1-\frac{2M}{r}\right)\mathrm{d}t^2 + \left(1-\frac{2M}{r}\right)^{-1}\mathrm{d}r^2 + r^2\left(\mathrm{d}\theta^2 + \sin^2\theta\,\mathrm{d}\varphi^2\right). \tag{1.3}$$

Here, $t$, $r$, $\theta$ and $\varphi$ are the Schwarzschild spacetime coordinates – analogous to traditional spherical coordinates in flat spacetime – and $M$ is the *mass of the solution*.

One of the interesting features of this solution is the presence of an *event horizon* at the so called Schwarzschild radius $r_S = 2M$. At this radius, the Schwarzschild metric (1.3) appears to be singular, as $g_{tt} \to 0$ and $g_{rr} \to \infty$. In fact, this is a coordinate singularity, not a physical one. At this boundary, when moving from the exterior region $r > r_S$ to the interior region $r < r_S$, the time coordinate $t$ and the radial coordinate $r$ reverse roles: $t$ turns into a spacelike coordinate as $g_{tt} > 0$, and $r$ becomes timelike, as $g_{rr} > 0$. This means that if an observer falls through the Schwarzschild radius, they will inevitably keep falling to $r \to 0$, just as inevitably as one grows from baby to adult as time passes. Due to this character flipping of the coordinates $r$ and $t$, the *future light cones* – which determine the set of events causally influenced by a point in spacetime – tip over, making it so that the interior region is *causally disconnected* from the exterior (this can be readily seen in Kruskal-Szekeres coordinates [4, 5]). These characteristics led John Wheeler to coin the term *Black Hole* to classify these kinds of objects: regions of spacetime where the gravitational pull is so strong that nothing, not even light, can escape.

Despite its impressive and counter-intuitive features, the Schwarzschild metric is only an idealized solution. The Schwarzschild black hole can be obtained from the collapse of a static, uncharged, spherically symmetric star. However, in nature, stars are neither static nor spherically symmetric, and they can also be (positively or negatively) charged. Therefore, generalisations of the Schwarzschild metric are in order.

In 1916 and 1918, respectively, Hans Reissner [6] and Gunnar Nördstrom [7] independently discovered a solution to the Einstein-Maxwell field equations describing the geometry of a spherically symmetric spacetime with charge $Q$ and mass $M$, aptly named the Reissner-Nordström solution. Many years later, in 1963, Roy Kerr [8] produced the metric for a neutral, spinning spacetime, which is referred to as the Kerr solution. Finally, in 1965, Ezra Newman put together together the works of Reissner, Nordström and Kerr and discovered the solution for an axisymetric spacetime describing a rotating and charged black hole. The Kerr-Newman line element reads

$$\mathrm{d}s^2 = -\frac{\Delta}{\Sigma}\left(\mathrm{d}t - a\sin^2\theta\,\mathrm{d}\varphi\right)^2 + \frac{\sin^2\theta}{\Sigma}\left[\left(r^2+a^2\right)\mathrm{d}\varphi - a\,\mathrm{d}t\right]^2 + \frac{\Sigma}{\Delta}\mathrm{d}r^2 + \Sigma\mathrm{d}\theta^2, \tag{1.4}$$

where

$$\Delta \equiv r^2 - 2Mr + a^2 + Q^2, \tag{1.5a}$$

$$\Sigma \equiv r^2 + a^2\cos^2\theta, \tag{1.5b}$$

$$a \equiv S/M, \tag{1.5c}$$

$(t, r, \theta, \varphi)$ are the Boyer-Lindquist coordinates – a generalisation of the Schwarzschild coordinates – and

$M$, $S$ and $Q$ are the mass, charge and angular momentum of the solution, respectively. In this work, we shall focus exclusively on electrically neutral solutions, *i.e.* those with $Q = 0$, corresponding to the Kerr family.

Kerr-Newman black holes exhibit remarkable features. One such feature is *frame-dragging*, a phenomenon in which objects are made to co-rotate with the black hole. For $r < r_0$, where

$$r_0 = M + \sqrt{M^2 - Q^2 - a^2 \cos^2 \theta}, \tag{1.6}$$

the so called *static limit*, no observer can stay at rest, and is forced by the geometry to orbit the black hole in the direction in which the latter rotates. The metric (1.4) also possesses an event horizon at $r = r_+$, with

$$r_+ = M + \sqrt{M^2 - Q^2 - a^2}. \tag{1.7}$$

This surface has similar characteristics to the one that appears in the Schwarzschild solution. The region between the static limit (1.6) and the event horizon (1.7) is called *ergoregion*. The Kerr-Newman metric (1.4) is conjectured to be the most general axisymmetric solution to the Einstein-Maxwell equations, an idea supported by a series of theorems by Carter [9], Hawking [10, 11] and Israel [12, 13]. This conjecture is well known as the *no-hair property* of black holes, which means there are no extra degrees of freedom – other than mass, charge and spin – relevant for the description a black hole.

We are now over a century from the publication of the field equations (1.2), and a lot of progress has been made in this field. General Relativity has passed – with flying colours – several experimental tests. The first one was performed by British astronomers Frank Watson Dyson and Arthur Stanley Eddington in 1919 [14], who measured the deflection of starlight during a solar eclipse on the 29th of May. More recently, in 2016, the LIGO Scientific Collaboration announced the first observation of *gravitational waves* from a binary black hole merger [15], not only confirming another notable prediction of General Relativity, but also starting a new era of multi-messenger observational astronomy. Just three years after, in 2019, the Event Horizon Telescope published the first ever picture of the shadow of a black hole [16], caused by the gravitational deflection of light and the capture of photons at the event horizon. This image, shown in Figure 1.1, is easily one of the most iconic scientific pictures of the last one hundred years.

However, General Relativity has also shown that there's a lot happening in the universe that we don't understand. An example of this is the *dark matter* problem. As it stands, the general relativistic description of gravity would not be able to hold the galaxies we observe together with just the matter we can detect. The theorised solution to this problem is the existence of a new kind of matter that does not emit or reflect electromagnetic radiation – in other words, *dark* matter. There are multiple dark matter candidates in the literature, but no definite conclusion has been reached yet about the nature of this mysterious substance.

Beyond their incredible simplicity in General Relativity, black holes are hosts to various fascinating phenomena, some of which were already discussed in the paragraphs above. One such effect, that has been a very active field of research for the past few decades, is that of *superradiance*.

Figure 1.1: Image of the shadow of the black hole at the core of the galaxy M87, using a $1.3\,\mathrm{mm}$ wavelength signal. Credit: Event Horizon Telescope Collaboration.

From etymology alone, one can understand that superradiance is a phenomenon through which radiation is enhanced. It is a general occurrence in physics, spanning the areas of quantum mechanics, optics and, more importantly to the scope of this thesis, black hole physics.

The study of superradiance can be traced back to 1929, in the early days of quantum mechanics, when Klein showed that the Dirac equation allowed for the propagation of electrons through potential barriers without the expected exponential damping, as long as the barrier was large enough [18]. This became known as the *Klein paradox*. It was later shown, by Hund, that pair creation of charged particles, described by the Klein-Gordon equation, happened at the potential barrier [19]. Further results in modern quantum field theory have shown that the solution to Klein's paradox is this mechanism of particle-antiparticle pair creation.

Superradiance is also present in classical systems, as was shown by Zel'dovich in 1972 [20]. In that work, the author studied the amplification of $m$-pole electromagnetic waves, of the form $\psi \propto e^{-i\omega t+im\varphi}$, from a rotating cylinder. He concluded that the condition for the wave to be superradiantly scattered by the rotating cylinder is that the rotational velocity of the object is greater than the phase velocity of the wave in the $\varphi$ direction, *i.e.*

$$\omega > m\Omega, \tag{1.8}$$

where $\omega$ is the angular frequency of the wave, $m$ is the azimuthal number and $\Omega$ is the velocity of the cylinder.

For black holes, the theory is slightly more complex. However, for some perturbation $\psi \propto e^{-i\omega t+im\varphi}$, be it scalar, Dirac spinor, electromagnetic or gravitational, the key result of equation (1.8) still holds, where $\Omega$ now represents the rotational velocity of the horizon of a Kerr black hole. For linear perturbations, *i.e.* without considering the backreaction of the perturbation onto the metric, it can be shown that complying with condition (1.8) leads to a negative energy flux through the horizon. Therefore, energy is extracted from the black hole by the perturbing field, amplifying it. When a confinement mechanism is in place, as is the case when dealing with massive perturbations, the energy extraction will persist and the

perturbing field will grow exponentially, giving rise to a *superradiant instability*. Such an event has been nicknamed *black hole bomb* in the literature. For a recent, complete review on the matter, see [17].

The subject of black hole superradiance has a number of interesting applications in theoretical physics. For example, studying astrophysical systems where superradiant instabilities are present may help us in searching for physics beyond the Standard Model, such as the search for dark matter. Furthermore, it can also be related to the formation of new, *hairy* black hole solutions, where the *hair* corresponds to the perturbative degrees of freedom, and it can shed some light onto problems of particle physics and condensed matter physics, such as spontaneous symmetry breaking and superfluidity, through the AdS/CFT correspondence [21–23].

General Relativity, by itself, is already quite a complex subject, and analytic solutions to the field equations (1.2) are, for the most part, impossible to find, unless in cases where strict spacetime symmetries are present – spherical or axial symmetry, static or stationary spacetimes. If one, then, tries to couple fundamental fields to the field equations, adding to the complexity of the problem, the only hope is to study the system numerically. We enter the realm of *Numerical Relativity*.

The numerical study of Einstein's equations was pioneered in the 1960s, through the works of Hahn and Lindquist [24], Smarr [25] and Eppley [26], who obtained the first numerical spacetimes in General Relativity. From then on, the field grew massively, alongside the evolution in power and accessibility of computers, not only allowing a deeper theoretical understanding of the mechanisms of gravity in Einstein's theory, but also providing state of the art experimental facilities – such as LIGO – with ways to extract meaningful information from very faint and noisy signals.

There are several different approaches to numerically solve the Einstein equations, which differ in the way the original field equations are transformed into computer-friendly expressions. The most widely used approach, and the one in which this thesis will be focused on, is the *3+1 Formalism* [27–29]. Within this formalism, spacetime is foliated in 3-dimensional slices of constant coordinate time, and the metric quantities are evolved from one slice to the next. Other approaches include the characteristic formulation [30], the conformal field equations [31] or the generalised harmonic decomposition [32].

In the black hole solutions of equations (1.3) and (1.4), the coordinates used are of spherical-type. These spacetimes have particular symmetries – spherical symmetry in the case of Schwarzschild, and axial symmetry in the case of Kerr-Newman – which makes it natural to write the line elements in spherical-type coordinates. However, for numerical evolution purposes, this is not the most common approach. Most Numerical Relativity codes make use of Cartesian coordinates, such as the very popular Einstein Toolkit [33].

Cartesian coordinates are particularly well-suited for numerical evolution, as they are regular everywhere, *i.e.* every physical location corresponds to a single value of the coordinates. This is not the case in spherical coordinates. For example, in the polar axis $\theta = 0$, for a definite value of $r$, any value of $\varphi$ corresponds to the same point. This is also the case at the origin $r = 0$, where the angular coordinates are redundant. Furthermore, spherical coordinates introduce coordinate singularities wherever $r \sin\theta = 0$, as differential operators and vector/tensor component expressions are typically inversely proportional to

some power of this factor.

However, apart from the obvious fact that they are better adapted to most problems in Numerical Relativity, spherical coordinates also result in numerical grids in which the number of points per unit angle is constant. Therefore, spherical coordinate grids have a higher resolution near the origin, where, in most cases, the interesting phenomena are located, and a much lower resolution towards the edges of the grid, thus saving memory and processor time in numerical simulations. This does not happen in Cartesian coordinates. One, then, is forced to use mechanisms such as mesh refinement in order to manage computational resources, but these introduce noise at the boundaries between grids.

There are now ways to deal with the problems that come with using spherical coordinates in Numerical Relativity, such as the use of reference-metrics to rescale tensorial quantities and avoid coordinate singularities. An example of a code that uses this approach is NRPy+ [34], that aims to implement machine-generation of code in Cartesian-, spherical- or cylindrical-type coordinates to solve the Einstein equations. This will be the focus of this thesis.

## 1.2 Objectives

This thesis aims to study, in the framework of Numerical Relativity, the evolution of fundamental scalar fields in black hole spacetimes, in the fully non-linear regimes, in general coordinate systems – in particular, in spherical-type coordinates. This shall be done through the implementation, within the NRPy+ infrastructure, of a module for coupling the BSSN evolution equations to those of the scalar fields. The main goals are to test the results against those present in the literature, obtained through numerical evolutions in Cartesian coordinates, thus validating the observed phenomena, as well as to demonstrate the improvement of numerical error when using coordinates adapted to the geometry.

## 1.3 Thesis Outline

The present thesis is structured as follows. In Chapter 2 we give an abbreviated, but self-contained, introduction to the techniques of Numerical Relativity, focusing on the 3+1 Formalism, the BSSN equations and the choices of coordinates. Then, in Chapter 3, we address the challenges that arise when one tries to use Numerical Relativity in curvilinear coordinate systems by introducing a covariant formulation of the BSSN equations, a tensor rescaling technique, and we provide an overview of the features of NRPy+, the code used in this work for numerical evolutions. In Chapter 4 we start by presenting the initial data used for construction of black hole spacetimes within NRPy+, demonstrating the convergence of numerical solutions. We also describe the initial data and evolution equations for scalar fields in these geometries, the implementation of these into the pre-existing NRPy+ code, and new convergence tests for these initial data. Finally, at the end of the chapter, we present the results of our evolutions of massless and massive scalar fields in Schwarzschild and Kerr spacetimes, analysing the behaviour of the scalar clouds as well as the gravitational wave signal. We present the conclusions of this work in Chapter 5.

# Chapter 2

# Numerical Relativity in a nutshell

Numerical Relativity is the name given to the field of physics that uses numerical methods, taking advantage of high performance computing systems, to study otherwise inaccessible dynamical phenomena under the framework of General Relativity, and extensions thereof. The usual approach, and the one taken in this work, is to set up a Cauchy problem, wherein initial data at time $t = 0$ for the spacetime is provided and, through the use of the Method of Lines, data for later times is obtained.

There is, however, an obvious problem with what is described above. Einstein's equations (1.2) are fully covariant, and there is no meaningful distinction between space and time. Therefore, the equations must be properly recast into a form well-suited for such numerical evolutions. This is a non-trivial task, which will be summarised throughout this chapter.

We shall first sketch the derivation of the so-called 3+1 form of the field equations in section 2.1. Then, in section 2.2 we analyse the shortcomings of the previous model, and present a widely used reformulation that addresses these issues: the BSSN scheme. Finally, in section 2.3 we provide insight on ways to take advantage of the coordinate freedom of General Relativity to obtain stable numerical evolutions.

## 2.1 The 3+1 Formalism: from Einstein to ADM

The 3+1 formalism is an approach which takes the covariant Einstein equations (1.2) and sets them up as a Cauchy problem. It does so by *foliating* the spacetime into 3-dimensional spacelike slices $\Sigma$, which evolve through a time coordinate. This is advantageous from a numerical point of view, as the formulation of a Cauchy problem allows for the use of standard methods to solve partial differential equations on computers. It does, however, come at a cost of diminishing the mathematical beauty and flexibility of the original formulation of GR.

This formulation has its roots between the 1920s and 1950s, in the works of Darmois [35], Lichnerowicz [36–38] and Choquet-Bruhat [39, 40]. In the late 1950s, Arnowitt, Deser and Misner (ADM) developed a Hamiltonian approach to General Relativity [41], which aimed at deriving evolution equations for the metric quantities. Later, York established the 3+1 equations in the way that became standard

in Numerical Relativity [42].

To develop the 3+1 formalism, the first step is to establish a *foliation*. Consider a spacetime manifold $\mathcal{M}$, which is 4-dimensional and endowed with a metric tensor $g_{ab}$. A foliation is a family of spacelike hypersurfaces $\{\Sigma_t\}, t \in \mathbb{R}$ such that each hypersurface corresponds to a level surface of a scalar field $t$, which acts as a global time function. In each slice of the foliation we can define the future-directed unit normal vector $n^a$ as

$$n^a = -\alpha \nabla^a t, \tag{2.1}$$

where $\alpha$ is the *lapse* function, $\nabla^a = g^{ab}\nabla_b$ and $\nabla_b$ is the covariant derivative compatible with the metric $g_{ab}$. This allows us to obtain the spatial metric induced by $g_{ab}$ on $\Sigma_t$ by

$$\gamma_{ab} = g_{ab} + n_a n_b. \tag{2.2}$$

By raising an index of the spatial metric we obtain a projection operator $\gamma^a_b$ which, when acting on a vector (or one-form) returns a purely spatial object, *i.e.* for some vector $V^a$,

$$n_a \gamma^a_b V^b = 0. \tag{2.3}$$

The extension to a general rank tensor is trivially obtained by contracting each index with a projection operator $\gamma^a_b$.

It is important to define a covariant derivative that is compatible with the spatial metric $\gamma_{ab}$. This can be done by projecting the spacetime covariant derivative $\nabla_a$ onto $\Sigma_t$, *i.e.*, for a scalar function $f$, we have

$$D_a f = \gamma^b_a \nabla_b f, \tag{2.4}$$

with trivial extensions to arbitrary rank spatial tensors. From this covariant derivative we can obtain 3-dimensional Christoffel symbols and the 3-dimensional Riemman tensor by the usual expressions, replacing $g_{ab}$ with $\gamma_{ab}$ everywhere.

The Riemann tensor we can obtain from the spatial metric $\gamma_{ab}$, just like its 4-dimensional counterpart, expresses the *intrinsic* curvature of the spacelike slice $\Sigma_t$. However, it holds no information about how the hypersurface is embedded into the spacetime $\mathcal{M}$. That information is contained in the *extrinsic curvature* tensor $K_{ab}$, defined by

$$K_{ab} = -\frac{1}{2}\mathcal{L}_n \gamma_{ab}, \tag{2.5}$$

where $\mathcal{L}_n$ is the Lie derivative along $n^a$. With $n^a$ being a timelike, future-pointing vector, $K_{ab}$ has the physical interpretation of a *time derivative* of the spatial metric.

We now have the basic ingredients to start deriving the 3+1 Einstein equations. To do that, we note that the original field equations (1.2) relate contractions of the Riemman curvature tensor with the stress energy tensor. Therefore, a natural path is to express the left-hand side of (1.2) in terms of the 3-dimensional Riemann tensor, the extrinsic curvature and other quantities mentioned above, and perform multiple projections using the projection operator $\gamma^a_b$ and the future-pointing unit vector $n_a$.

There are three non-vanishing contractions of the Riemann tensor with the projection operator: the full spatial projection on all four indices, the projection with one index contracted with $n^a$, and the projection with two indices contracted with the normal vector. For the sake of brevity, the full derivation will not be presented here, but the results will be summarised.

The full projection of the 4-dimensional Riemann tensor ${}^{(4)}R_{abcd}$ onto $\Sigma_t$ gives the *Gauss equation*,

$$\gamma_a^p \gamma_b^q \gamma_c^r \gamma_d^s \, {}^{(4)}R_{pqrs} = R_{abcd} + K_{ac}K_{bd} - K_{ad}K_{cb}. \tag{2.6}$$

Projecting one of the indices of ${}^{(4)}R_{abcd}$ onto the normal direction holds the *Codazzi equation*,

$$\gamma_a^p \gamma_b^q \gamma_c^r n^s \, {}^{(4)}R_{pqrs} = D_b K_{ac} - D_a K_{bc}. \tag{2.7}$$

Finally, contracting twice with $n^a$ gives the *Ricci equation*,

$$\gamma_a^p \gamma_b^q n^r n^s \, {}^{(4)}R_{pqrs} = \mathcal{L}_n K_{ab} + \alpha^{-1} D_a D_b \alpha + K_b^c K_{ac}. \tag{2.8}$$

This set of equations is usually referred to as the *Gauss-Codazzi equations*.

Notice that the Ricci equation (2.8) includes a term featuring the Lie derivative along $n^a$ of the extrinsic curvature. Just like in equation (2.5), the definition of the extrinsic curvature, this has the physical interpretation of a time evolution equation for the extrinsic curvature. It is also worth noting the relations above are purely geometric: nowhere in the derivation were Einstein's equations used.

To carry on towards the goal of the 3+1 form of the field equations, we now need to transform the Gauss-Codazzi equations by replacing the 4-dimensional Riemann tensor in the right-hand side of equations (2.6), (2.7) and (2.8), with the help of Einstein's equations.

First, we contract the Gauss equation on two indices, and define the energy density $\rho$ measured by an observer with 4-velocity $n^a$ – hereafter referred to as a *normal observer* – as

$$\rho = n_a n_b T^{ab}. \tag{2.9}$$

What we obtain is the *Hamiltonian constraint*,

$$R + K^2 - K_{ab}K^{ab} = 16\pi\rho, \tag{2.10}$$

where $R$ is the 3-dimensional Ricci scalar and $K = g^{ab}K_{ab}$ is the trace of the extrinsic curvature.

By contracting the Codazzi equation once and defining the momentum density $S_a$ measured by a normal observer,

$$S_a = -\gamma_a^b n^c T_{bc}, \tag{2.11}$$

we obtain the *momentum constraint*,

$$D_b K_a^b - D_a K = 8\pi S_a. \tag{2.12}$$

In order to obtain a useful relation from the Ricci equation, we first define the vector $t^a$ given by

$$t^a = \alpha n^a + \beta^a, \tag{2.13}$$

where $\beta^a$ is the spatial *shift* vector. This vector is dual to $\nabla_a t$, *i.e.*

$$t^a \nabla_a t = 1. \tag{2.14}$$

By the rules following from the definition of the Lie derivative, we are able to write

$$\mathcal{L}_t K_{ab} = \alpha \mathcal{L}_n K_{ab} + \mathcal{L}_\beta K_{ab}, \tag{2.15}$$

which is a more natural time derivative candidate then $\mathcal{L}_n K_{ab}$.

One can now introduce (2.15) into the Ricci equation (2.8). By defining the spatial stress tensor and its trace as

$$S_{ab} = \gamma_a^c \gamma_b^d T_{cd} \quad \text{and} \quad S = g^{ab} S_{ab}, \tag{2.16}$$

and further simplifying, making use of Einstein's equations and the Gauss relation, we obtain the evolution equation for the extrinsic curvature,

$$\mathcal{L}_t K_{ab} = -D_a D_b \alpha + \alpha \left( R_{ab} - 2K_{ac} K_b^c + K K_{ab} \right) - 8\pi\alpha \left[ S_{ab} - \frac{1}{2} \gamma_{ab} \left( S - \rho \right) \right] + \mathcal{L}_\beta K_{ab}. \tag{2.17}$$

Going back to the definition of the extrinsic curvature, equation (2.5), and making the substitution in equation (2.15), we obtain the evolution equation for the spatial metric,

$$\mathcal{L}_t \gamma_{ab} = -2\alpha K_{ab} + \mathcal{L}_\beta \gamma_{ab}. \tag{2.18}$$

Equations (2.10), (2.12), (2.17) and (2.18) are equivalent to Einstein's equations (1.2). They are clearly divided in two sets: the Hamiltonian and momentum constraints, as their name suggests, have nothing to do with time evolution of the system, but rather with how $\Sigma_t$ is embedded in $\mathcal{M}$ for each coordinate time $t$; the evolution equations are the ones that push the fundamental variables – the spatial metric $\gamma_{ab}$ and the extrinsic curvature $K_{ab}$ – forward in time.

Throughout the discussion above, all tensors were written is abstract index notation, making all quantities coordinate independent. However, it can be shown that, by choosing $t^a$, as defined in (2.13), as the zeroth basis vector of the coordinate system, the Lie derivatives that appear in the evolution equations can be simplified to partial derivatives, and timelike components of spatial tensors can be ignored without loss of information.

By doing this, we find the expression for the unit normal vector $n^a$ and the shift vector $\beta^a$,

$$n^a = \alpha^{-1} \left( 1, -\beta^i \right) \quad \text{and} \quad \beta^a = \left( 0, \beta^i \right). \tag{2.19}$$

Furthermore, it is possible to prove that $\gamma_{ik}\gamma^{kj} = \delta_i^j$, meaning we can raise or lower spatial indices with the 3-metric. We can write the 3+1 line element as

$$\mathrm{d}s^2 = -\alpha^2 \mathrm{d}t^2 + \gamma_{ij}\left(\mathrm{d}x^i + \beta^i \mathrm{d}t\right)\left(\mathrm{d}x^j + \beta^j \mathrm{d}t\right). \tag{2.20}$$

The roles of the lapse function $\alpha$ and the shift vector $\beta^i$ can be understood from the above discussion. The lapse tells us how much proper time elapses for a Eulerian observer – *i.e.* an observer with 4-velocity $n^a$ – when going from a hypersurface $\Sigma_t$ to another $\Sigma_{t+\mathrm{d}t}$ separated by an infinitesimal amount of coordinate time $\mathrm{d}t$. The shift vector, on the other hand, lets us know how much the local coordinates change, *i.e.* get shifted, when moving from one slice to the next, with respect to the normal vector $n^a$. These variables encode the coordinate freedom of General Relativity in the 3+1 formalism, which will be explored later in this chapter.

One important point of the discussion above is that all information contained in a spatial tensor can be attained from spatial components alone. We can, then, rewrite the 3+1 equations to a form that is known as often referred to as the ADM form of the Einstein field equations:

$$R + K^2 - K_{ij}K^{ij} = 16\pi\rho, \tag{2.21a}$$

$$D_j\left(K^{ij} - \gamma^{ij}K\right) = 8\pi S^i, \tag{2.21b}$$

$$\begin{aligned}\partial_t K_{ij} =& -D_i D_j \alpha + \alpha\left(R_{ij} - 2K_{ik}K^k_j + KK_{ij}\right) - 8\pi\alpha\left[S_{ij} - \frac{1}{2}\gamma_{ij}\left(S - \rho\right)\right] \\ &+ \beta^k D_k K_{ij} + K_{ik}D_j\beta^k + K_{kj}D_i\beta^k,\end{aligned} \tag{2.21c}$$

$$\partial_t \gamma_{ij} = -2\alpha K_{ij} + D_i\beta_j + D_j\beta_i. \tag{2.21d}$$

## 2.2 The BSSN Formulation

In the previous section we decomposed the Einstein field equations (1.2) into their 3+1 form, clearly separating time from space. What we ended up with, system (2.21), amounts to two constraint equations (2.21a, 2.21b), which we must solve to obtain physically significant initial data, and two evolution equations (2.21c, 2.21d), for the extrinsic curvature $K_{ij}$ and the spatial metric $\gamma_{ij}$, to step our system forward in time. It can be shown that the evolution equations preserve the constraints, *i.e.* if the constraints are satisfied initially, and the system is evolved using the evolution equations, then the constraints will remain unviolated throughout the whole evolution – at least analytically.

One would then think we are well-equipped to jump on the computer and evolve the ADM equations to obtain numerical solutions to dynamical spacetimes in General Relativity. However, in most cases of full 3+1 numerical evolution, what happens in practice is that for any non-trivial spacetime, the evolutions are unstable, quickly causing overflows and crashing the codes. This can sometimes be avoided by working in spacetimes with high degrees of symmetry, like spherical or axial symmetry, but that is not

the goal of Numerical Relativity in general, or of this work in particular.

The reason for the instabilities in numerical evolution is actually a formal one. Let us start by defining well-posedness. Consider a set $u$ of $n$ variables in a $(d+1)$-dimensional spacetime. The evolution equations for $u$ read

$$\partial_t u + A^i \partial_i u = S, \tag{2.22}$$

where $A^i$ are $n \times n$ matrices, and the index $i$ represents each spatial dimension, running from 1 to $d$. Suppose we provide initial data at $t = 0$ of the form $u\left(0, x^i\right)$. We say the initial value problem is well-posed if it is possible to define a norm $\|\cdot\|$ such that

$$\left\|u\left(t, x^i\right)\right\| \leq k e^{\alpha t} \left\|u\left(0, x^i\right)\right\| \tag{2.23}$$

for every $t \geq 0$, where $k$ and $\alpha$ are constants that do not depend on the initial data. That is, the system is well-posed if it is bounded by an exponential for all $t$. This is useful in numerical evolution, as one does not want the computational variables to grow indefinitely, producing overflows, loss of information, or ultimately causing the code to crash.

To understand the well-posedness – or ill-posedness – of the ADM equations, it is instructive to define the concept of hyperbolicity. Consider again a system like that of equation (2.22), and build a matrix $P = A^i n_i$, where $n^i$ is some unit vector. This matrix is called the *principal symbol* of the system. If, for all unit vectors $n^i$, $P$ has a complete set of eigenvectors corresponding to real eigenvalues, we say the system is *strongly hyperbolic*. On the other hand, if $P$ has real eigenvalues, but its eigenvectors do not generate the whole space, the system is only *weakly hyperbolic*. It can be shown that initial value problems defined by strongly hyperbolic systems are well-posed, whilst those defined from weakly hyperbolic ones are ill-posed.

The ADM form of the Einstein equations, as derived in section 2.1, is only weakly hyperbolic. For a proof of this statement, see, for example, chapter 5 of Alcubierre's book [28]. It is clear now that the instability of numerical evolutions is caused by the ill-posedness of the system. However, there are several formulations, based on the previous approach, that take the system (2.21) to a strongly hyperbolic form. The most notable of these is the BSSN formulation, presented in 1995 by Shibata and Nakamura [43] and further developed and tested, in the context of Numerical Relativity, by Baumgarte and Shapiro [44].

The first step towards the construction of the BSSN equations is the conformal rescaling of the spatial metric. Let $\psi$ be a positive function of the coordinates, henceforth named the *conformal factor*. We can write $\gamma_{ij}$ as

$$\gamma_{ij} = \psi^4 \bar{\gamma}_{ij}, \tag{2.24}$$

where $\bar{\gamma}_{ij}$ is some *conformally related metric*, or *conformal metric* for short. The obvious relation for the inverse metric holds,

$$\gamma^{ij} = \psi^{-4} \bar{\gamma}^{ij}. \tag{2.25}$$

For the BSSN formulation, it is customary to rewrite the conformal factor as $\psi = e^{\phi}$, so that the confor-

mally related metric is given by

$$\bar{\gamma}_{ij} = e^{-4\phi}\gamma_{ij}. \tag{2.26}$$

Furthermore, we choose $\phi$ in such a way that makes the determinant of the conformally related metric $\bar{\gamma}$ equal to that of the flat metric $\eta$. This gives

$$\phi = \frac{1}{12}\ln\left(\frac{\gamma}{\eta}\right). \tag{2.27}$$

In Cartesian coordinates, we have $\bar{\gamma} = \eta = 1$. We will assume the use of this coordinate system throughout this section.

In regards to the extrinsic curvature, we first split it into a traceless part $A_{ij}$ and its trace $K$ in the following way:

$$K_{ij} = A_{ij} + \frac{1}{3}\gamma_{ij}K. \tag{2.28}$$

The conformal transformation rules for these quantities are quite arbitrary, and they should be done in a way that facilitates the solution of the constraints. In BSSN, the choice is to rescale the trace-free part in the same manner as the spatial metric, *i.e.*

$$\bar{A}_{ij} = e^{-4\phi}A_{ij}. \tag{2.29}$$

The trace $K$ is not rescaled using the conformal factor.

Defining $\bar{D}_i$ as the covariant derivative associated with the conformally related metric, the Christoffel symbols transform as

$$\Gamma^i_{jk} = \bar{\Gamma}^i_{jk} + 2\left(\delta^i_j\bar{D}_k\phi + \delta^i_k\bar{D}_j\phi - \bar{\gamma}_{jk}\bar{\gamma}^{il}\bar{D}_l\phi\right), \tag{2.30}$$

and the Ricci tensor becomes

$$R_{ij} = \bar{R}_{ij} - 2\left(\bar{D}_i\bar{D}_j\phi + \bar{\gamma}_{ij}\bar{\gamma}^{lm}\bar{D}_l\bar{D}_m\phi\right) + 4\left(\bar{D}_i\phi\bar{D}_j\phi - \bar{\gamma}_{ij}\bar{\gamma}^{lm}\bar{D}_l\phi\bar{D}_m\phi\right). \tag{2.31}$$

The secret to transforming the ADM equations into a strongly hyperbolic system lies in eliminating the mixed second derivatives, *i.e.* terms such as $\partial^k\partial_i\bar{\gamma}_{kj}$. Terms like these appear in the expression for the conformally related Ricci tensor $\bar{R}_{ij}$ when the expression for $R_{ij}$ is introduced and the spatial metric is replaced by its conformally related cousin. We can avoid the appearance of these terms by defining a contraction of the Christoffel symbols, sometimes called *conformal connection functions*, as

$$\bar{\Gamma}^i = \bar{\gamma}^{jk}\bar{\Gamma}^i_{jk} = -\partial_j\bar{\gamma}^{ij}. \tag{2.32}$$

Using the conformal connection functions, the Ricci tensor can be written as

$$\bar{R}_{ij} = -\frac{1}{2}\bar{\gamma}^{lm}\partial_m\partial_l\bar{\gamma}_{ij} + \bar{\gamma}_{k(i}\partial_{j)}\bar{\Gamma}^k + \bar{\Gamma}^k\bar{\Gamma}_{(ij)k} + \bar{\gamma}^{lm}\left(2\bar{\Gamma}^k_{l(i}\bar{\Gamma}_{j)km} + \bar{\Gamma}^k_{im}\bar{\Gamma}_{klj}\right). \tag{2.33}$$

In this expression there are no mixed second derivatives, as intended. The only second derivative

present is the Laplacian $\bar{\gamma}^{lm}\partial_m\partial_l$.

To complete this effort, we need obtain the constraints and evolution equations written in terms of the new variables. Firstly, we can split the evolution equation for the spatial metric (2.21d) into one for the conformal factor,

$$\partial_t\phi = -\frac{1}{6}\alpha K + \beta^i\partial_i\phi + \frac{1}{6}\partial_i\beta^i, \tag{2.34a}$$

and an equation for the conformally related metric,

$$\partial_t\bar{\gamma}_{ij} = -2\alpha\bar{A}_{ij} + \beta^k\partial_k\bar{\gamma}_{ij} + \bar{\gamma}_{ik}\partial_j\beta^k + \bar{\gamma}_{kj}\partial_i\beta^k - \frac{2}{3}\bar{\gamma}_{ij}\partial_k\beta^k. \tag{2.34b}$$

By performing the conformal traceless decomposition of the extrinsic curvature, using equation (2.28), we can split the evolution equation for $K_{ij}$ (2.21c) into an equation for the trace,

$$\partial_t K = -\gamma^{ij}D_jD_i\alpha + \alpha\left(\bar{A}_{ij}\bar{A}^{ij} + \frac{1}{3}K^2\right) + 4\pi\alpha\left(\rho + S\right) + \beta^i\partial_i K, \tag{2.34c}$$

and another for the traceless part,

$$\begin{aligned}\partial_t\bar{A}_{ij} =& e^{-4\phi}\left[-\left(D_iD_j\alpha\right)^{\mathsf{TF}} + \alpha\left(R_{ij}^{\mathsf{TF}} - 8\pi S_{ij}^{\mathsf{TF}}\right)\right] + \alpha\left(K\bar{A}_{ij} - 2\bar{A}_{il}\bar{A}^l_j\right)\\ &+ \beta^k\partial_k\bar{A}_{ij} + \bar{A}_{ik}\partial_j\beta^k + \bar{A}_{kj}\partial_i\beta^k - \frac{2}{3}\bar{A}_{ij}\partial_k\beta^k.\end{aligned} \tag{2.34d}$$

Here, variables that do not correspond to the conformally related ones should be substituted accordingly. Elevating the conformal connection functions $\bar{\Gamma}^i$ to variables to evolve alongside the ones above, we can obtain their evolution equations, which read

$$\begin{aligned}\partial_t\bar{\Gamma}^i =& -2\bar{A}^{ij}\partial_j\alpha + 2\alpha\left(\bar{\Gamma}^i_{jk}\bar{A}^{kj} - \frac{2}{3}\bar{\gamma}^{ij}\partial_j K - 8\pi\bar{\gamma}^{ij}S_j + 6\bar{A}^{ij}\partial_j\phi\right)\\ &+ \beta^j\partial_j\bar{\Gamma}^i - \bar{\Gamma}^j\partial_j\beta^i + \frac{2}{3}\bar{\Gamma}^i\partial_j\beta_j + \frac{1}{3}\bar{\gamma}^{li}\partial_l\partial_j\beta^j + \bar{\gamma}^{lj}\partial_j\partial_l\beta^i.\end{aligned} \tag{2.34e}$$

Finally, the constraint equations are also altered in the BSSN formulation. The new expression for the Hamiltonian constraint is [45]

$$\mathcal{H} \equiv \frac{2}{3}K^2 - \bar{A}_{ij}\bar{A}^{ij} + e^{-4\phi}\left(\bar{R} - 8\bar{\gamma}^{ij}\bar{D}_j\phi\bar{D}_i\phi - 8\bar{\gamma}^{ij}\bar{D}_j\bar{D}_i\phi\right) - 16\pi\rho = 0 \tag{2.34f}$$

and the momentum constraint reads

$$\mathcal{M}^i \equiv e^{-4\phi}\left(\bar{D}_j\bar{A}^{ij} + 6\bar{A}^{ij}\bar{D}_j\phi - \frac{2}{3}\bar{\gamma}^{ij}\bar{D}_jK\right) = 0 \tag{2.34g}$$

Equations (2.34) constitute the full BSSN evolution scheme for the Einstein field equations in 3+1 form. It can be shown that, as was the intention all along, the equations are strongly hyperbolic and combine to a well-posed system. Once again, the proof of this statement can be found, for example, in reference [28].

Since its development, at the end of the 1990s, the BSSN formalism has been used in most full 3+1

dimensional numerical evolutions of spacetimes in General Relativity and extensions thereof. Paired with adequate initial data and gauge conditions, it provides the framework for much longer evolutions than the ADM equations. However, it does have some drawbacks, such as the fact that it was derived specifically with Cartesian coordinates in mind. These coordinates are certainly the most common in 3+1 Numerical Relativity, as they are in general simpler to implement than, say, spherical polar coordinates. However, they are usually not the natural coordinate system for most situations of interest in General Relativity, *i.e.* they are not adapted to the exact or approximate symmetries of the problem at hand. We will go into more detail on this issue in the next chapter.

## 2.3 Coordinate freedom

The freedom to choose coordinates or, in other words, the coordinate-independence of the field equations (1.2), is a defining feature of General Relativity as a theory. That feature carries over to the 3+1 formalism and its extensions, like the BSSN scheme of the previous section, through the gauge variables: the lapse $\alpha$ and the shift $\beta^i$. The choice of gauge is a non-trivial issue, as it might break the stability of the equations under computational evolution. Therefore, it has been a major part of the research surrounding the numerical solution of Einstein's equations. In this section, we mention a few important options for gauge fixing, as well as some of their most important features.

The simplest possible choice one can make for the gauge variables is the so-called *geodesic slicing*, in which the lapse and shift have fixed values throughout the whole evolution, given by

$$\alpha = 1 \quad \text{and} \quad \beta^i = 0. \tag{2.35}$$

It can be shown that the acceleration of normal observers in this gauge is zero. Hence, normal observers follow geodesics in these coordinates, justifying the name.

However simple, geodesic slicing is not well-suited to numerical evolution. In non-trivial spacetimes, the curvature might focus geodesics into small regions, or single points if singularities are present. As the coordinates are adapted to the geodesics, coordinate singularities will form, and overflows or underflows might occur, spoiling the numerical evolution. Therefore, for anything other than flat spacetimes, which are of little interest to Numerical Relativity, geodesic slicing does not present itself as a wise choice of gauge.

Another possible choice of gauge is, surprisingly, not defined through fixing the gauge functions themselves. Instead, in *maximal slicing*, one fixes the trace of the extrinsic curvature to

$$K = 0. \tag{2.36}$$

If this holds for all $t$, the time derivative of $K$ also vanishes. This allows us to write a condition for the lapse from a contraction of the ADM equation (2.21c), which reads

$$D^i D_i \alpha = \alpha \left[ K_{ij} K^{ij} + 4\pi \left( \rho + S \right) \right]. \tag{2.37}$$

The shift can be chosen independently of $\alpha$.

The advantages of using the maximal slicing gauge for the lapse amount to its singularity avoidance property. It can be shown that, in this gauge, normal observers have zero expansion, meaning that distances between normal observers are preserved and no coordinate singularities form. However, equation (2.37) for $\alpha$ is an elliptic equation that is computationally hard to solve during an evolution. In this case, specific techniques for elliptic equations must be employed at each time step, which differ from the ones used for the hyperbolic evolution equations of the BSSN scheme. Therefore, it might be useful to find a gauge that provides an hyperbolic equation for the lapse and shift, so they can be evolved in equal footing with relation to the remaining variables.

A gauge option that solves the issue brought up by maximal slicing can be obtained by providing conditions to the Christoffel symbols. Specifically, let ${}^{(4)}\Gamma^a$ be the following contraction of the Christoffel symbols:

$$ {}^{(4)}\Gamma^a = g^{bc}\, {}^{(4)}\Gamma^a_{bc}. \tag{2.38} $$

By setting the zeroth component of ${}^{(4)}\Gamma^a$ to zero, and assuming a vanishing shift, one obtains an evolution equation for the lapse, namely

$$ \partial_t \alpha = -\alpha^2 K. \tag{2.39} $$

This condition is referred to as the *harmonic slicing* condition. It can be generalised through the use of some function $f(\alpha)$ such that the evolution equation becomes

$$ \partial_t \alpha = -\alpha^2 f(\alpha) K. \tag{2.40} $$

A particularly relevant form of this generalised harmonic slicing gauge is obtained when setting $f(\alpha) = 2/\alpha$, which gives

$$ \partial_t \alpha = -2\alpha K, \tag{2.41} $$

the notable *1+log* slicing condition.

Like maximal slicing, these conditions have a singularity avoidance property. However, it is weaker than in the previous case. Nevertheless, this gauge choice for the lapse has been the go-to for several types of simulations in Numerical Relativity, including binary black hole evolutions.

We now work towards obtaining conditions for the spatial coordinates, through the gauge choice of the shift vector, as opposed to the slicing conditions described above, which relate to the time coordinate. One example of such a choice is called the *minimal distortion* gauge, and it is based on minimising the time derivative of the conformally related metric, $\partial_t \bar{\gamma}_{ij}$. It can be shown that this leads to an elliptic equation for the shift, which reads

$$ D^j D_j \beta^i + \frac{1}{3} D^i D_j \beta^j + R^i_j \beta^j = 16\pi \alpha S^i + \frac{4}{3} \alpha D^i K + 2A^{ij} D_j \alpha, \tag{2.42} $$

or, in terms of the conformally related metric and the conformal factor $\psi$,

$$\bar{D}^i \left(\psi^6 \partial_t \bar{\gamma}_{ij}\right) = 0. \tag{2.43}$$

Physically, this gauge choice minimises variations in the metric which are due to the change of the coordinates themselves, thus letting the evolution focus on the change of the actual geometry. However, just like the maximal slicing condition (2.37), it provides us with an elliptic equation for a gauge quantity, which must be solved at each time step of the evolution. This takes a heavy toll on computational resources, making simulations longer.

Alternatives to the minimal distortion gauge can be achieved by providing an evolution equation to $\beta^i$. A successful example of this is the *hyperbolic gamma driver*, where the second time derivative of $\beta^i$ is proportional to the time derivative of the conformal connection functions defined in equation (2.32). Since this is a second order PDE on $\beta^i$, in analogy to what was done with the spatial metric and extrinsic curvature, we define an auxiliary variable $B^i$ such that

$$\partial_t \beta^i = \frac{3}{4} B^i. \tag{2.44a}$$

Then, we set the time derivative of this auxiliary variable to

$$\partial_t B^i = \partial_t \bar{\Gamma}^i - \eta B^i, \tag{2.44b}$$

where $\eta$ is a freely specifiable damping parameter that helps prevent the appearance of strong oscillations in the shift.

The 1+log condition for the lapse (2.41) together with the gamma driver condition for the shift (2.44) are the most common gauge choices in Numerical Relativity, and are thus usually referred to as *the standard gauge*. This conjunction was proposed by Alcubierre *et al.* [46] as a way to enable stable evolutions of black hole spacetime without excision. Later, van Meter *et al.* [47] investigated the propagation of low-speed oscillation modes under this gauge, which could lead to the accumulation of numerical error within the grid. With this in mind, they proposed generalising the standard gauge by subtracting a shift advection term, of the form $\beta^i \partial_i$, to each time derivative appearing in Equations (2.41) and (2.44). The new evolution equations for $\alpha$ and $\beta^i$ read

$$\left(\partial_t - \beta^i \partial_i\right) \alpha = -2\alpha K, \tag{2.45a}$$

$$\left(\partial_t - \beta^j \partial_j\right) \beta^i = \frac{3}{4} B^i, \tag{2.45b}$$

$$\left(\partial_t - \beta^j \partial_j\right) B^i = \left(\partial_t - \beta^j \partial_j\right) \bar{\Gamma}^i - \eta B^i. \tag{2.45c}$$

In this work, we will be using a modified version of the gauge evolution equations above, which will be detailed and justified in the next chapter.

# Chapter 3

# BSSN in curvilinear coordinates and NRPy+

In the previous chapter we derived the BSSN formalism, a powerful evolution scheme for the 3+1 form of Einstein's equations. The BSSN equations have been used extensively for several years now in most 3+1 evolutions in Cartesian coordinates, the most common coordinate choice in Numerical Relativity.

Cartesian coordinates are very well suited to numerical evolution. For starters, there is no ambiguity as to where the coordinates point in physical space: every set of coordinate values corresponds to one and only one physical location. Furthermore, there are no coordinate singularities for this choice of coordinates. However, many problems in physics have symmetries which make the Cartesian system not ideal. Examples like the evolution of a single Kerr-Newman black hole (1.4) are naturally described in spherical polar coordinates.

Spherical polar coordinates and, in general, other curvilinear coordinate systems, suffer from afflictions that might hinder numerical evolution. Contrary to Cartesian coordinates, in spherical coordinates we find that $\theta$ and $\varphi$ are periodic. Thus, an infinite number of values of $\theta$, for example, correspond to the same point. To further complicate matters, there are coordinate singularities at the origin and on the polar axis, where $r \sin\theta = 0$. This is problematic because differential operators, as well as tensor components, in spherical coordinates are inversely proportional to factors that become zero at these points, causing potential overflows in numerical evolution.

In order to circumvent these issues, one first needs to rewrite the BSSN scheme in a covariant form, which has been done by Brown [48]. Then, the coordinate singularities described above need to be taken care of, and this might be done either by adopting a Partially Implicit Runge-Kutta method, as developed by Cordero-Carrión and Cerdá-Durán [49], or by rescaling vector and tensor components with the appropriate quantities, eliminating the divergences analytically [34].

In this chapter we go through the Covariant BSSN Formulation, in section 3.1, defining new variables and deriving their equations of motion for numerical evolution. Next, in section 3.2, we explain the tensor rescaling procedure that allows us to analytically treat the coordinate singularities present in vector and tensor quantities that would otherwise spoil numerical evolution. Finally, in section 3.3 and

the subsections therein, we introduce NRPy+ [34], a Python infrastructure aimed at code generation for Numerical Relativity simulations.

## 3.1 Covariant BSSN Formulation

The derivation of the BSSN scheme in section 2.2 of this thesis assumed, as stated, the use of Cartesian coordinates, in particular by assuming that $\bar{\gamma} = \eta = 1$. This equation is covariant if we consider the conformally related metric to be a tensor density of weight $2/3$. However, the resulting coordinate transformation relations are quite cumbersome to work with.

Pairing the BSSN equations with the standard gauge (2.41, 2.44) only makes matters worse. Focusing on equation (2.44b), it can easily be seen that the term $\partial_t \bar{\Gamma}^i$ is not covariant, since the conformal connection functions are built from the Christoffel symbols, which do not transform as tensors.

To solve this issue, we first introduce a time-independent background metric $\hat{\gamma}_{ij}$, which we take to be the flat metric in whatever coordinates are chosen, and write the conformal spatial metric as

$$\bar{\gamma}_{ij} = \hat{\gamma}_{ij} + \varepsilon_{ij}. \tag{3.1}$$

The conformal metric is related to the physical spatial metric by the usual relation (2.26), where $\phi$ is now given more generally by

$$\phi = \frac{1}{12} \ln \left( \frac{\gamma}{\bar{\gamma}} \right). \tag{3.2}$$

Now instead of imposing that $\bar{\gamma} = \eta$, we instead provide an evolution equation to $\bar{\gamma}$, namely by using Brown's Lagrangian evolution equation

$$\partial_t \bar{\gamma} = 0. \tag{3.3}$$

This allows all the tensorial quantities present in the formalism to transform as regular tensors, instead of tensor densities.

The non-covariance of the conformal connection functions, pointed out above, can also be taken care of by noticing that, even though Christoffel symbols do not transform as tensors, the difference between two sets of them does. With this in mind, we define

$$\Delta^i_{jk} = \bar{\Gamma}^i_{jk} - \hat{\Gamma}^i_{jk}, \tag{3.4}$$

and contract this tensor with the conformal metric,

$$\Delta^i = \bar{\gamma}^{jk} \Delta^i_{jk}. \tag{3.5}$$

The contraction $\Delta^i$ allows us to define a new independently evolved vector $\bar{\Lambda}^i$, which is equal to $\Delta^i$ when the constraint

$$\mathcal{C} = \bar{\Lambda}^i - \Delta^i = 0 \tag{3.6}$$

holds.

Using the above, it is possible to rewrite the evolution equations of the BSSN scheme (2.34) in terms of a combination of new variables – $\varepsilon_{ij}$ and $\bar{\Lambda}^i$ – and old ones – $\bar{A}_{ij}$, $\phi$ and $K$. This yields

$$(\partial_t - \mathcal{L}_\beta)\,\varepsilon_{ij} = \frac{2}{3}\bar{\gamma}_{ij}\left(\alpha\bar{A}^k_k - \bar{D}_k\beta^k\right) + 2\hat{D}_{(i}\,\beta_{j)} - 2\alpha\bar{A}_{ij}, \tag{3.7a}$$

$$\begin{aligned}(\partial_t - \mathcal{L}_\beta)\,\bar{A}_{ij} = &-\frac{2}{3}\bar{A}_{ij}\bar{D}_k\beta^k - 2\alpha\bar{A}_{ik}\bar{A}^k_j + \alpha\bar{A}_{ij}K \\ &+ e^{-4\phi}\left[-2\alpha\bar{D}_i\bar{D}_j\phi + 4\alpha\bar{D}_i\phi\bar{D}_j\phi + 4\bar{D}_{(i}\,\alpha\bar{D}_{j)}\phi - \bar{D}_i\bar{D}_j\alpha + \alpha\bar{R}_{ij}\right]^{\mathsf{TF}},\end{aligned} \tag{3.7b}$$

$$(\partial_t - \mathcal{L}_\beta)\,\phi = \frac{1}{6}\left(\bar{D}_k\beta^k - \alpha K\right), \tag{3.7c}$$

$$(\partial_t - \mathcal{L}_\beta)\,K = \frac{1}{3}\alpha K^2 + \alpha\bar{A}_{ij}\bar{A}^{ij} - e^{-4\phi}\left(\bar{D}^i\bar{D}_i\alpha + 2\bar{D}^i\alpha\bar{D}_i\phi\right), \tag{3.7d}$$

$$(\partial_t - \mathcal{L}_\beta)\,\bar{\Lambda}^i = \bar{\gamma}^{jk}\hat{D}_j\hat{D}_k\beta^i + \frac{2}{3}\Delta^i\bar{D}_j\beta^j + \frac{1}{3}\bar{D}^i\bar{D}_j\beta^j - 2\bar{A}^{ij}\left(\partial_j\alpha - 6\partial_j\phi\right) + 2\bar{A}^{jk}\Delta^i_{jk} - \frac{4}{3}\alpha\bar{\gamma}^{ij}\partial_j K. \tag{3.7e}$$

The Ricci tensor can now be computed through

$$\bar{R}_{ij} = -\frac{1}{2}\bar{\gamma}^{kl}\hat{D}_k\hat{D}_l\bar{\gamma}_{ij} + \bar{\gamma}_{k(i}\,\hat{D}_{j)}\bar{\Lambda}^k + \Delta^k\Delta_{(ij)k} + \bar{\gamma}^{kl}\left[2\Delta^m_{k(i}\,\Delta_{j)ml} + \Delta^m_{ik}\Delta_{mjl}\right]. \tag{3.8}$$

All there is left to do is to fix the Gamma-driver evolution equation for the auxiliary vector $B^i$. This is done by replacing $\partial_t\bar{\Gamma}^i$ by $\partial_t\bar{\Lambda}^i$, giving the system[1]

$$\left(\partial_t - \beta^j\partial_j\right)\beta^i = B^i, \tag{3.9a}$$

$$\left(\partial_t - \beta^j\partial_j\right)B^i = \frac{3}{4}\left(\partial_t - \beta^j\partial_j\right)\bar{\Lambda}^i - \eta B^i. \tag{3.9b}$$

Adding the 1+log evolution equation for the lapse (2.41) we obtain the full set of evolution equations for all important quantities. This set must, of course, be complemented with the constraint equations (2.34f, 2.34g) so that the field equations (1.2) are completely satisfied.

## 3.2 Tensor rescaling

Another issue that needs tackling when one intends to solve Einstein's equation numerically on a general curvilinear grid is the presence of singular coefficients in both tensor component expressions and differential operators. To illustrate this problem, consider a generic vector field with components $V^i$. The vector may be expressed in a Cartesian coordinate basis $\frac{\boldsymbol{\partial}}{\boldsymbol{\partial x^i}}$ as

$$\boldsymbol{V} = V^i\frac{\boldsymbol{\partial}}{\boldsymbol{\partial x^i}}. \tag{3.10}$$

[1] Note that $\eta$ in equation 3.9b does not correspond to the determinant of the flat metric, but is instead a damping parameter for the gamma driver evolution equations.

If we wish to express this vector field in spherical coordinates $x'^i = (r, \theta, \varphi)$ instead of Cartesian coordinates $x^i = (x, y, z)$, tensor transformation rules give the expression

$$\boldsymbol{V} = \frac{\partial x'^i}{\partial x^j} V^j \frac{\boldsymbol{\partial}}{\boldsymbol{\partial x'^j}}. \tag{3.11}$$

Consider the particular case where only the $x$ component of $\boldsymbol{V}$, $V^x$, is non-zero. Then, the factors $\frac{\partial x'^i}{\partial x}$ in (3.11) can be computed from the usual relations between $x^i$ and $x'^i$, yielding in the spherical coordinate basis $\frac{\boldsymbol{\partial}}{\boldsymbol{\partial x'^i}}$

$$\boldsymbol{V} = V^x \sin\theta\cos\varphi \frac{\boldsymbol{\partial}}{\boldsymbol{\partial r}} + V^x \frac{\cos\theta\cos\varphi}{r} \frac{\boldsymbol{\partial}}{\boldsymbol{\partial \theta}} - V^x \frac{\sin\varphi}{r\sin\theta} \frac{\boldsymbol{\partial}}{\boldsymbol{\partial \varphi}}. \tag{3.12}$$

As can be seen, this transformation results in coordinate singularities wherever $r\sin\theta = 0$. This is undesirable in a numerical context, as the divergence and rapid variation of these tensor components require the use of significantly more points to approximate spatial derivatives through finite differences in a satisfactory way.

Fortunately, this complication can be easily averted with tensor rescaling. This technique, as presented by Ruchlin, Etienne and Baumgarte [34], relies on defining a non-coordinate basis that incorporates the singular terms, thus ridding the tensor components of their divergent behaviour. For the example above, we can define three non-coordinate basis vectors, namely

$$\boldsymbol{e}_{(r)} = \frac{\boldsymbol{\partial}}{\boldsymbol{\partial r}}, \quad \boldsymbol{e}_{(\theta)} = \frac{1}{r}\frac{\boldsymbol{\partial}}{\boldsymbol{\partial \theta}} \quad \text{and} \quad \boldsymbol{e}_{(\varphi)} = \frac{1}{r\sin\theta}\frac{\boldsymbol{\partial}}{\boldsymbol{\partial \varphi}}, \tag{3.13}$$

and rewrite the vector $\boldsymbol{V}$ in terms of this basis as

$$\boldsymbol{V} = V^x \sin\theta\cos\varphi\, \boldsymbol{e}_{(r)} + V^x \cos\theta\cos\varphi\, \boldsymbol{e}_{(\theta)} - V^x \sin\varphi\, \boldsymbol{e}_{(\varphi)}. \tag{3.14}$$

This procedure can be easily generalised to arbitrary coordinate systems as follows. Consider a non-coordinate basis vectors $e^i_{(j)}$, where the index in parenthesis denotes each of the basis vectors, and the index without parenthesis refers to the components of the individual vector. The non-coordinate basis vectors are related to the coordinate basis $\frac{\boldsymbol{\partial}}{\boldsymbol{\partial x^i}}$ through the so-called *orthogonal scale factors* $F_i$, by the relation

$$\boldsymbol{e}_{(i)} = \frac{1}{F_i}\frac{\boldsymbol{\partial}}{\boldsymbol{\partial x^i}} \tag{3.15}$$

The dual basis $e^{(i)}_j$ can be obtained, as usual, by

$$e^{(i)}_k e^k_{(j)} = e^{(k)}_j e^i_{(k)} = \delta^i_j. \tag{3.16}$$

The reference metric can be expressed in terms of the non-coordinate basis vectors as

$$\hat{\gamma}_{ij} = \delta_{kl} e^{(k)}_i e^{(l)}_j, \tag{3.17}$$

which is taken to be the defining relation for the scale factors $F_i$. In orthogonal coordinate systems, onto which we focus our efforts, and if the reference metric is taken to be that of flat space, the only non-zero elements of $\hat{\gamma}_{ij}$ are along its diagonal. Therefore, we can compute the $F_i$ by simply taking the square root of each diagonal element of the reference metric, *i.e.*

$$F_i = \sqrt{\hat{\gamma}_{ii}}, \tag{3.18}$$

where there is no implied sum over the repeated $i$ index on the right-hand side.

For arbitrary rank tensors, the rescaling procedure amounts to contracting each contravariant, or covariant, component of the tensor with a non-coordinate basis vector, or dual vector, respectively. As an example, for a type-$\binom{2}{1}$ tensor $\boldsymbol{T}$, the components of its rescaled sibling $\boldsymbol{t}$ are given by

$$t^{ij}_{k} = T^{mn}_{l} e^{(i)}_{m} e^{(j)}_{n} e^{l}_{(k)}. \tag{3.19}$$

With this technique, we can define rescaled versions of the tensors and vectors to be evolved through our covariant BSSN scheme of equations (3.7). We, therefore, define the quantities $h_{ij}$, $a_{ij}$, $\lambda^i$, $\mathcal{V}^i$ and $\mathcal{B}^i$ as

$$h_{ij} = \varepsilon_{kl} e^{k}_{(i)} e^{l}_{(j)}, \tag{3.20a}$$

$$a_{ij} = \bar{A}_{kl} e^{k}_{(i)} e^{l}_{(j)}, \tag{3.20b}$$

$$\lambda^i = \bar{\Lambda}^k e^{(i)}_{k}, \tag{3.20c}$$

$$\mathcal{V}^i = \beta^k e^{(i)}_{k}, \tag{3.20d}$$

$$\mathcal{B}^i = B^k e^{(i)}_{k}, \tag{3.20e}$$

and their respective evolution equations are obtained by the same rescaling.

## 3.3 NRPy+

In the previous sections of this chapter we built a framework that, in principle, will allow us to solve Einstein's equations, in 3+1 form, not only in Cartesian coordinates, but in more general *curvilinear* coordinate systems. In section 3.1 we went through the details of a covariant formulation of the BSSN scheme, derived in the last chapter. Then, noticing how some curvilinear coordinates might produce unphysical singularities in vector and tensor quantities, we introduced a tensor rescaling method in section 3.2, which allows us to evolve equations (3.7) without the worry of coordinate related overflows.

We are now ready to put this theoretical foundation to practice, proceeding to numerical simulation of spacetimes in Numerical Relativity. To that end, we introduce the NRPy+/SENR [34] infrastructure. NRPy+ is a Python-based package that aims to generate highly optimised C code to perform Numerical Relativity computations. This is done through the symbolic manipulation of expressions appearing, for example, in the right-hand sides of the evolution equations, using the standard, open-source Python

library *SymPy*. Using algorithms such as common subexpression elimination, NRPy+ outputs the expressions to C files, which are further optimised by using OpenMP parallelisation [50] and SIMD vectorisation. The files are then used by SENR ("the Simple, Efficient Numerical Relativity code"), which provides the essential structure to perform the evolutions.

In this section we will provide insight into the workings of NRPy+/SENR, explaining the procedures of setting up numerical grids, initial data and boundary conditions, how it handles time evolution and coordinates, and other important features.

### 3.3.1 Numerical grids

NRPy+'s way to solve Einstein's equations numerically is the so-called *Method of Lines*: the quantities to evolve are computed in a number of points of the computational domain, called the *grid points* , the right-hand side of the evolution equations (3.7) are evaluated at those same grid points, and the system is advanced in time by a small time step $\Delta t$. It is important to set up the numerical grid in a way that provides stable evolution and allows the user to probe the phenomena they are interested in.

Within NRPy+, the numerical grid coordinates are designated $\mathtt{x}^i = (\mathtt{x0}, \mathtt{x1}, \mathtt{x2})$. These do not always correspond to the physical coordinate values. Both their relation to physical coordinates and the ranges of values the numerical grid coordinates may take are related to the specific coordinate choice the user implements. However, in the numerical domain, they are always considered to be uniformly spaced, even if that does not translate to uniform spacing in the physical coordinates, as we shall see in the next section.

The number of grid points for each spatial direction, $N_i$, can be specified by the user. This allows NRPy+ to compute the spacing between two consecutive grid points in the $i$-th direction,

$$\Delta \mathtt{x}^i = \frac{\mathtt{x}^i_{\mathsf{max}} - \mathtt{x}^i_{\mathsf{min}}}{N_i}. \tag{3.21}$$

To approximate the spatial derivatives that feature in the evolution equations, one uses finite differences, which require the knowledge of the grid functions – *i.e.* the functions evaluated at the computational grid – at neighbouring points in the domain. This poses a problem for points near the boundaries of the grid, where there might not be neighbours. To tackle this issue, a number of *ghost points*, $N_{\mathsf{G}}$, is added at each boundary of the domain, obeying special boundary conditions. The number of ghost points is related to the order of finite differences used, $N_{\mathsf{FD}}$, by the relation

$$N_{\mathsf{G}} = \frac{N_{\mathsf{FD}}}{2} + 1. \tag{3.22}$$

Both the finite difference methods and the boundary conditions will be discussed in upcoming sections.

Since we intend to use curvilinear coordinate systems that, in some cases, introduce singularities in the grid functions, it is important to choose the locations of our grid points in a way that avoids such divergent behaviour. This is done through cell-centred grids, in which the $j$-th point in the $i$-th direction

has numerical coordinates

$$\mathtt{x}^i_j = \Delta\mathtt{x}^i \left( j - N_{\mathsf{G}} + \frac{1}{2} \right), \tag{3.23}$$

where $j$ varies from 0 to the total number of points $N_{\mathsf{T}i}$ in that direction,

$$N_{\mathsf{T}i} = N_i + 2N_{\mathsf{G}}. \tag{3.24}$$

Points given by relation (3.23) that lie outside the computational domain, to either side, correspond to the ghost points.

### 3.3.2 Coordinates

Through the use of the reference metric, covariant BSSN formulation of equations (3.7), NRPy+ allows for the generation of code to solve Einstein's equation in curvilinear coordinates. Some of the most used coordinate systems, namely Cartesian-, spherical- and cylindrical-like coordinates, are already implemented in the package. Depending on the choice of coordinate system, NRPy+ defines the reference metric $\hat{\gamma}_{ij}$, as well as the related Christoffel symbols $\hat{\Gamma}^i_{jk}$ and scale factors.

The most simple coordinate system within NRPy+ is, obviously, the Cartesian one. In this system, the three spatial coordinates $x^i = (x, y, z)$ correspond directly to the computational grid coordinates, which we denote by $\mathtt{x}^i = (\mathtt{x0}, \mathtt{x1}, \mathtt{x2})$. The values of the $\mathtt{x}^i$ range between $\mathtt{x}^i_{\mathsf{min}}$ and $\mathtt{x}^i_{\mathsf{max}}$, where the minimum and maximum values can be set by the user for each of the coordinates independently. In Cartesian coordinates, the reference metric is the identity matrix,

$$\hat{\gamma}_{ij} = \begin{pmatrix} 1 & 0 & 0 \\ 0 & 1 & 0 \\ 0 & 0 & 1 \end{pmatrix}, \tag{3.25}$$

and the scalar factors are all unity.

However, as has been stated multiple times throughout this thesis, our goal is to evolve spacetimes of General Relativity in spherical-like coordinates. Fortunately, these are also available to use in NRPy+. Spherical-like coordinates $x^i = (r, \theta, \varphi)$ are related to their Cartesian counterparts by the usual relations,

$$x = r \sin\theta \cos\varphi, \tag{3.26a}$$

$$y = r \sin\theta \sin\varphi, \tag{3.26b}$$

$$z = r \cos\theta. \tag{3.26c}$$

Contrary to Cartesian coordinates, in spherical-like systems the grid coordinates $\mathtt{x}^i$ don't always correspond exactly to the physical coordinates. It is possible that this is the case, if one chooses to use the traditional spherical coordinate system, in which $r \in [0, R_{\mathsf{max}}]$, $\theta \in [0, \pi]$ and $\varphi \in [-\pi, \pi]$. However, one can take $r \equiv f(\mathtt{x0})$, where $f$ is an odd function of $\mathtt{x0}$, in which case $\mathtt{x0} \in [0, 1]$. One example of such

coordinates is called the *SinhSpherical* coordinate system, where

$$r = R_{\text{max}} \frac{\sinh\left(\frac{\mathrm{x0}}{w_s}\right)}{\sinh\left(\frac{1}{w_s}\right)}. \tag{3.27}$$

This acts as a non-trivial map of the grid coordinate $\mathrm{x0}$ to the interval $[0, R_{\text{max}}]$ in the physical radial coordinate $r$. An advantage of such a coordinate system is to push the computational boundary further away from the origin, whilst maintaining high resolution in the strong-field region.

In spherical-like coordinates, the reference metric is given by

$$\hat{\gamma}_{ij} = \begin{pmatrix} 1 & 0 & 0 \\ 0 & r^2 & 0 \\ 0 & 0 & r^2 \sin^2\theta \end{pmatrix}, \tag{3.28}$$

and the scale factors are the numerical coefficients appearing in the non-coordinate basis vectors of relation (3.13). NRPy+ also implements other rescalings of $r$ as a function of the computational coordinate $\mathrm{x0}$, as well as a cylindrical coordinate option, but those will not be mentioned here since they won't be utilised.

### 3.3.3 Initial data

The first step to the solution of a Cauchy problem is to provide data for all the grid functions at an initial time $t = 0$. In NRPy+ there are already several modules that implement initial data for useful spacetime configurations. Amongst these modules are Static Trumpet [51] data for a single Schwarzschild Black Hole, the UIUC [52] data for a single rotating Kerr Black Hole, the Brill-Lindquist [53] data for a system of two non-rotating Black Holes, or the data for a Tolman–Oppenheimer–Volkoff (TOV) [54, 55] star. Apart from the modules already provided, a user is always able to define their own initial data routines. There are two ways to provide initial data: analytically or numerically.

In the analytical case, *SymPy* symbolic expressions for the ADM – the spatial metric $\gamma_{ij}$ and the extrinsic curvature $K_{ij}$ – and for the gauge variables – the lapse $\alpha$ and the shift $\beta^i$ – are given. These can be written in either Cartesian or spherical coordinates. As an example, the Static Trumpet and the UIUC Black Hole modules are written in spherical coordinates, but the Brill-Lindquist module uses Cartesian coordinates instead. NRPy+ will, then, convert these expressions into initial data for the covariant BSSN variables (3.20) in the coordinate system the user desires.

Sometimes, however, it is not possible to find analytical solutions to the constraint equations. This is the case, for example, in the case of the initial data for a TOV star. In such cases, one solves the constraints numerically, resulting in text files containing the ADM data. This data is, then, interpolated and converted into covariant BSSN form, with any spatial derivatives appearing in the conversion computed through finite differences, rather than symbolically.

### 3.3.4 Spatial derivatives

Spatial derivatives of the evolved quantities (3.20) appear throughout our covariant BSSN formalism, be it in initial data expressions or the evolution equations themselves. Throughout the evolution, the grid functions do not follow a closed-form expression, making symbolic derivation impossible. Therefore, as briefly mentioned in the sections above, *finite difference methods* are used to approximate these derivatives.

Take $u(x)$ to be a function of a single variable $x$. Then, its derivative is defined by

$$u'(x) = \lim_{\Delta x \to 0} \frac{u(x + \Delta x) - u(x)}{\Delta x}. \tag{3.29}$$

If one samples $u$ in a discrete computational grid, like the one employed in Method of Lines numerical evolutions of Einstein's equations, there is no way to take this limit. In this case, $\Delta x$ has a minimum value set by the minimum distance between grid points adjacent to $x$. However, if $\Delta x$ is small, the derivative can be approximated by the *finite difference* quotient

$$u'(x) \approx \frac{u(x + \Delta x) - u(x)}{\Delta x}. \tag{3.30}$$

Expression (3.30) above, however, does not provide the most universal finite difference method. In general, a finite difference approximation to the derivative $u'(x)$ is given by

$$u'(x) \approx \sum_k a_k u(x_k), \tag{3.31}$$

where $a_k$ are finite difference coefficients and the index $k$ runs over a number of points $x_k$ in the vicinity of $x$. Two questions emerge from this expression: how to choose the points $x_k$ and how to compute the finite difference coefficients.

The most widespread way to solve both of these issues is through Taylor series expansions of $u(x)$ in the grid points near the point of interest. The Taylor series of $u$ around some point $x_0$ has the form

$$u(x) = \sum_{k=0}^{\infty} \frac{u^{(k)}(x_0)}{n!} (x - x_0)^k, \tag{3.32}$$

where $u^{(k)}(x_0)$ is the $k$-th derivative of $u$ with respect to $x$ at the point $x_0$. Now let $N_{\mathsf{FD}}$ be an even number, $n = N_{\mathsf{FD}}/2$ and $X = \{x_{-n}, ..., x_0, ..., x_n\}$ the set of points around $x_0$, including the central point. If one writes $u(x), x \in X$ as a Taylor series around $x_0$, one is left with a set of equations which can be linearly combined together, and solved to yield an expression for the derivative $u'(x_0)$. In fact, approximate expressions for higher order derivatives are easily obtainable through this process. From Taylor's theorem, it can be shown that this method of approximating derivatives is accurate to order $N_{\mathsf{FD}}$ in the spacing between grid points $\Delta x$.

This procedure can be applied in a general way to arbitrary *finite difference approximation order* $N_{\mathsf{FD}}$ and for derivatives of any order. As an example, let us see how it works for a 4th order approximation of

$u'(x_0)$. In the notation used above, $X = \{x_{-2}, x_{-1}, x_0, x_1, x_2\}$. Consider also that the points are evenly spaced with distance $\Delta x$ between consecutive points, such that $x_i = x_0 + i\Delta x$. Denoting $u(x_i) \equiv u_i$, we can expand $u$ in a Taylor series at each point, yielding

$$u_{-2} = u_0 \; - (2\Delta x)\, u_0' + \frac{(2\Delta x)^2}{2} u_0'' - \frac{(2\Delta x)^3}{3!} u_0^{(3)} + \frac{(2\Delta x)^4}{4!} u_0^{(4)} + \mathcal{O}\left((\Delta x)^5\right), \tag{3.33a}$$

$$u_{-1} = u_0 \; - (\Delta x)\, u_0' \; + \frac{(\Delta x)^2}{2} u_0'' \; - \frac{(\Delta x)^3}{3!} u_0^{(3)} \; + \frac{(\Delta x)^4}{4!} u_0^{(4)} \; + \mathcal{O}\left((\Delta x)^5\right), \tag{3.33b}$$

$$u_0 = u_0, \tag{3.33c}$$

$$u_1 = u_0 \; + (\Delta x)\, u_0' \; + \frac{(\Delta x)^2}{2} u_0'' \; + \frac{(\Delta x)^3}{3!} u_0^{(3)} \; + \frac{(\Delta x)^4}{4!} u_0^{(4)} \; + \mathcal{O}\left((\Delta x)^5\right), \tag{3.33d}$$

$$u_2 = u_0 \; + (2\Delta x)\, u_0' + \frac{(2\Delta x)^2}{2} u_0'' + \frac{(2\Delta x)^3}{3!} u_0^{(3)} + \frac{(2\Delta x)^4}{4!} u_0^{(4)} + \mathcal{O}\left((\Delta x)^5\right). \tag{3.33e}$$

The next step is to perform a linear combination of the equations above, such that

$$\frac{1}{\Delta x} \sum_k a_k u_k = u_0' + \mathcal{O}\left((\Delta x)^4\right). \tag{3.34}$$

By writing relation (3.34) in factors of the $k$-th order derivative of $u_0$, one can equate each of the factors accompanying $u_0^{(k)}$ to either 1, if $k = 1$, or 0 otherwise. Absorbing factors of $(\Delta x)^k$ into the derivative terms, the linear system we encounter can be written in matrix form as

$$\begin{pmatrix} 1 & 1 & 1 & 1 & 1 \\ (-2) & (-1) & 0 & 1 & 2 \\ (-2)^2 & (-1)^2 & 0 & 1 & 2^2 \\ (-2)^3 & (-1)^3 & 0 & 1 & 2^3 \\ (-2)^4 & (-1)^4 & 0 & 1 & 2^4 \end{pmatrix} \begin{pmatrix} a_{-2} \\ a_{-1} \\ a_0 \\ a_1 \\ a_2 \end{pmatrix} = \begin{pmatrix} 0 \\ 1 \\ 0 \\ 0 \\ 0 \end{pmatrix}. \tag{3.35}$$

Therefore, the problem of computing the finite difference coefficients $a_k$ amounts to the inversion of a matrix.

In NRPy+, the technique is applied to obtain expressions for spatial derivatives, appearing in the right-hand sides of the evolution equations (3.7), as well as to obtain initial data numerically, when derivatives can not be taken symbolically. The finite difference order $N_{\text{FD}}$ can be set to any positive even integer, and the number of ghost points $N_{\text{G}}$, introduced in section 3.3.1 is calculated accordingly.

### 3.3.5 Time-stepping

With the finite difference methods described in the previous section, we are now able to use equations (3.7) to step our system forward in time. Expressing the spatial derivatives as finite differences, the evolution equations become ordinary differential equations. The standard way to evolve systems of ODEs in time is to use *explicit Runge-Kutta methods* (henceforth we might drop the *explicit* designation, as no other methods shall be considered).

Let $u(t)$ be an unknown function of time $t$. Its evolution is given by the ODE

$$\frac{\mathrm{d}u}{\mathrm{d}t} = f(t,u), \tag{3.36}$$

where $f$ is some function. Using Runge-Kutta methods, one can take an small step in time, from $t_n$ to $t_{n+1} = t_n + \Delta t$. The function $u$ at the new time value will be given by

$$u_{n+1} = u_n + \Delta t \sum_{i=1}^{s} b_i k_i, \tag{3.37a}$$

where $u_n \equiv u(t_n)$. The $k_i$ can be seen as the values of $f(t,u)$ at intermediate time steps, and are given recursively by

$$k_i = f\left(t_n + c_i \Delta t, u_n + \Delta t \sum_{j=1}^{i-1} a_{ij} k_j\right). \tag{3.37b}$$

In equations (3.37a) and (3.37b), the $a_{ij}$, $b_i$ and $c_i$ are numerical coefficients. This coefficients are what makes the distinction between several types of Runge-Kutta methods, and they are usually visualised in a Butcher table:

$$\begin{array}{c|ccccc} 0 & & & & & \\ c_2 & a_{21} & & & & \\ c_3 & a_{31} & a_{32} & & & \\ \vdots & \vdots & & \ddots & & \\ c_s & a_{s_1} & a_{s2} & \cdots & a_{s,s-1} & \\ \hline & b_1 & b_2 & \cdots & b_{s-1} & b_s \end{array} \tag{3.37c}$$

The most used Runge-Kutta method, and the one used in this thesis, is the 4th order one, usually designated *RK4*. For this method, we have the expressions for the $k_i$ given by

$$k_1 = \Delta t\, f(u_n, t_n), \tag{3.38a}$$

$$k_2 = \Delta t\, f\left(u_n + \frac{1}{2}k_1, t_n + \frac{\Delta t}{2}\right), \tag{3.38b}$$

$$k_3 = \Delta_t\, f\left(u_n + \frac{1}{2}k_2, t_n + \frac{\Delta t}{2}\right), \tag{3.38c}$$

$$k_4 = \Delta t\, f(u_n + k_3, t_n + \Delta t). \tag{3.38d}$$

The profile of $u(t_{n+1})$ can be obtained from

$$u_{n+1} = u_n + \frac{1}{6}(k_1 + 2k_2 + 2k_3 + k_4), \tag{3.38e}$$

corresponding to the following Butcher table:

$$\begin{array}{c|cccc} 0 & & & & \\ 1/2 & 1/2 & & & \\ 1/2 & 0 & 1/2 & & \\ 1 & 0 & 0 & 1 & \\ \hline & 1/6 & 1/3 & 1/3 & 1/6 \end{array} \tag{3.38f}$$

The RK4 method described above is accurate to 4th order in the time step $\Delta t$.

The time evolution is supplemented at each time step by the application of boundary conditions and inner parity conditions, which will be described in detail in the next section. Furthermore, the $k_i$ substeps also need to be provided with adequate boundary and inner parity conditions. Finally, at each time step, the of the evolution, the Lagrangian condition for the evolution of the determinant of the conformally related spatial metric is enforced by making the substitution

$$\bar{\gamma}_{ij} \to \left(\frac{\hat{\gamma}}{\bar{\gamma}}\right) \bar{\gamma}_{ij} \tag{3.39}$$

where $\bar{\gamma}$ is the determinant of the spatial metric at the initial time $t = 0$.

### 3.3.6 Boundary conditions

Another key aspect that differs between Cartesian and general curvilinear coordinate systems, as far as finding a numerical solution to a Cauchy problem is concerned, is the application of boundary conditions. Indeed, in Cartesian coordinates, all numerical boundaries correspond to exterior boundaries of the physical system under study. This makes applying boundary conditions straightforward, as all the points in the boundary region suffer the same fate.

This is not the case, however, in curvilinear systems, where some coordinates might have a periodic behaviour, or some other symmetries. As an example, take the azimuthal angle $\varphi$ in a spherical coordinate system. The extremal points of the interval where $\varphi$ is defined, $\varphi = -\pi, \pi$, correspond to the same physical point, therefore constituting an *inner boundary*. Conversely, the radial coordinate $r$ at $r = R_{\text{max}}$ corresponds to a physical exterior limit of the system, which is thus classified as an *outer boundary*.

In a numerical evolution scenario, this difference is of paramount importance. Therefore, it is a necessity to establish what points lie on inner or outer boundaries, and how to assign data at the inner boundary points according to the periodic nature of the coordinates. Furthermore, vectors and tensors components must obey parity conditions when moving across an inner boundary, which must also be accounted for. The problem of implementing boundary conditions can, then, be divided into the following:

1. Identifying inner and outer boundary points;
2. Defining the parity conditions that vectors and tensors must obey when moving across inner boundaries;
3. Obtaining relations to determine the behaviour at outer boundaries.

To understand how to distinguish inner from outer boundaries, let us first describe what the aim is for these points. As explained in section 3.3.4, the approximation of spatial derivatives, using finite differences, requires the use of points in the vicinities of the point of interest. However, if the point of interest lies just inside a boundary, some neighbouring points will correspond to the ghost points, introduced in section 3.3.1. At the inner boundaries, due to the periodic nature of some coordinates, the ghost points will lie inside the numerical domain, superposed to the physical grid. The values of the grid functions must be corresponded between these ghosts and the inner points.

Consider relation (3.23) that establishes the coordinates of each grid point. Evidently, ghost points, where $j < N_{\mathsf{G}}$ or $j > N_i + N_{\mathsf{G}}$, have coordinate values that lie outside the established ranges. Take one of these ghost points, with coordinates $x^i_{\mathsf{gp}}$ in a general curvilinear coordinate system, which is utilised for numerical evolution. To find out whether this point lies on an inner or outer boundary of the computational domain, we express the location of the point in Cartesian coordinates, writing

$$(x, y, z) \equiv \left(x\left(x^i\right), y\left(x^i\right), z\left(x^i\right)\right). \tag{3.40}$$

Next, we transform back to the original system, obtaining

$$x^i_{\mathsf{new}} \equiv x^i_{\mathsf{new}}(x, y, z). \tag{3.41}$$

Two cases might occur: if $x^i_{\mathsf{gp}} = x^i_{\mathsf{new}}$, the ghost point belongs to an outer boundary; on the contrary, if $x^i_{\mathsf{gp}} \neq x^i_{\mathsf{new}}$, then it corresponds to an inner boundary.

Inner boundaries occur for coordinates with fixed domains – *i.e.* domains that are dependent only on the geometry of the coordinate system and cannot be defined by the user. This is what happens in the case of the angular coordinates $\theta$ and $\varphi$ in a spherical system, as opposed to the radial coordinate's upper limit, which can be set freely. Therefore, when a point has coordinate values that lie outside the domain of these domains, transforming to Cartesian coordinates and back will single out the non-trivial behaviour across the inner boundaries, returning the coordinate values inside the domain that correspond to the same physical location.

However, this technique can be tricky to implement in some cases. For example, in the case of spherical-like coordinates where the radial coordinate is given by equation (3.27), the relations that take $(r, \theta, \varphi) \to (x, y, z)$ are not invertible. The solution for this problem is to create an inner boundary mapping before the evolution starts, using what is designated in NRPy+ as an *Eigen-Coordinate System*. An Eigen-Coordinate System is a coordinate system where the relations (3.40) are invertible. In particular, for spherical-like coordinates, the Eigen-Coordinate system is the regular spherical one; for cylindrical-like coordinates, the Eigen-Coordinate system is the regular cylindrical one. In the Eigen-Coordinate system, the mappings of ghost points across inner boundaries to the interior points match the ones in the original system, with the advantage of not needing numerical methods to invert the transformations to Cartesian coordinates.

The next issue to address is that of defining parity conditions for scalar, vector and tensor variables across inner boundaries, which is done before the evolution, at grid setup time. This is done by deter-

mining the change in the unit vectors that define each direction when an inner boundary is crossed.

To better grasp what happens, consider, as has been usual throughout this thesis, a spherical coordinate system. Say we are going through the inner boundary at $\theta = \pi$. A ghost point beyond this boundary will have some coordinates

$$(r, \theta, \varphi)_{\text{gp}} = (r_0, \pi + \delta\theta, \varphi_0)\,. \tag{3.42}$$

This will, however, correspond to a physical point inside the domain, which, by the symmetries of the coordinate system, corresponds to a reflection in $\theta$ at $\theta = \pi$ and a translation in $\varphi$ by an amount $\pi$. The *new* coordinates, in accordance to the nomenclature defined above for ghost points, will be given by

$$(r, \theta, \varphi)_{\text{new}} = (r_0, \pi - \delta\theta, \varphi_0 + \pi)\,, \tag{3.43}$$

assuming no inner boundary in $\varphi$ is encountered. The unit basis vector $\frac{\boldsymbol{\partial}}{\boldsymbol{\partial\theta}}$, computed in each of the coordinate sets above, will give a different result – in particular, its direction will be reversed when going to the *new* coordinates. This change in direction will affect the components of a vector or tensor calculated across this boundary.

In general, when going across an inner boundary, the unit basis vectors $\frac{\boldsymbol{\partial}}{\boldsymbol{\partial x^i}}$ might flip their direction. This is easily probed if one takes the dot product between the vector in the ghost point coordinates and the *new* coordinates. Since these are unit vectors, the dot product will be either +1, if no change in direction happens, or -1, if indeed the vector changed direction. To this end, we define this dot product as

$$P_i = \frac{\boldsymbol{\partial}}{\boldsymbol{\partial x^i}}\left(x^j_{\text{gp}}\right) \cdot \frac{\boldsymbol{\partial}}{\boldsymbol{\partial x^i}}\left(x^j_{\text{new}}\right) = \pm 1. \tag{3.44}$$

This translates into parity relations for tensor components as follows. Consider a type-$\binom{n}{m}$ tensor $\boldsymbol{T}$. When crossing an inner boundary, the tensor components of a ghost point must be replaced by the ones at the corresponding physical point, which is found as described above. Furthermore, these components might suffer a parity change from the reversal of the unit vectors at that boundary. The overall substitution relation for the components of $\boldsymbol{T}$ is

$$T^{ijk...}_{lmn...}\left(x^a\right) = \left(\prod_\alpha P_\alpha\right) T^{ijk...}_{lmn...}\left(x^a_{\text{new}}\right), \quad \text{with} \quad \alpha \in \{i, j, k, ..., l, m, n...\}\,. \tag{3.45}$$

In practice, though, only scalars, vectors and rank-2 tensors are present in the covariant BSSN formalism. Therefore, it is not computationally hard to establish all possible parity relations for each grid function[2] type prior to the start of the numerical evolution. To that end, a set of 10 parity types, listed in Table 3.1, is considered.

The process of setting up the structure of the ghost points corresponding to inner boundaries is achieved as follows. At grid set up time, all ghost points are grouped into inner and outer boundary points, by the method described earlier in this section. At the same time, for the inner boundary points,

[2]Note that each tensor component is treated as a separate grid function in NRPy+.

| Tensor type | Parity type | Dot product | Example |
|---|---|---|---|
| Scalar | 0 | 1 | +1 |
| Rank 1, Direction 0 | 1 | $P_0$ | +1 |
| Rank 1, Direction 1 | 2 | $P_1$ | -1 |
| Rank 1, Direction 2 | 3 | $P_2$ | -1 |
| Rank 2, Direction 00 | 4 | $P_0^2$ | +1 |
| Rank 2, Direction 01 | 5 | $P_0 P_1$ | -1 |
| Rank 2, Direction 02 | 6 | $P_0 P_2$ | -1 |
| Rank 2, Direction 11 | 7 | $P_1^2$ | +1 |
| Rank 2, Direction 12 | 8 | $P_1 P_2$ | +1 |
| Rank 2, Direction 22 | 9 | $P_2^2$ | +1 |

Table 3.1: Parity types for BSSN variables in NRPy+. $P_i$ refers to the dot products of equation (3.44). The example column refers to the values of the dot products to its left when evaluated at a boundary where $\sin\theta = 0$ in spherical-like coordinates.

a map is created that matches the grid coordinates of the ghost point to those of the inner point it corresponds to. Finally, all listed parity types are given a value of $\pm 1$ for each of those inner ghost points. All this information is stored in a structure, so that it can be easily accessed during every step of the evolution, in which the parity conditions must be enforced. A second structure, consisting of the locations of the outer boundary points, is also created, so that one can effortlessly loop through them and apply boundary conditions during the evolution.

The last thing on the menu, regarding boundary conditions in NRPy+, is understanding what is done to the points at the outer boundary at every time step of the evolution. There are two main choices implemented in the code on this matter: the *Quadratic Polynomial Extrapolation* (QPE) method or the widely used *Sommerfeld* boundary conditions.

The QPE method is rather simple. With this method, the grid function values at ghost zone points are approximated, from the innermost layer outwards, by extrapolation with an order 2 polynomial, through expression

$$f(x) \approx 3f(x - \Delta x) - 3f(x - 2\Delta x) + f(x - 3\Delta x), \tag{3.46}$$

where $f$ is some grid function, $x$ is the coordinate perpendicular to the outer boundary, and $\Delta x$ is the distance between consecutive points in the $x$ direction. $\Delta x$ need not be constant; here, $x - n\Delta x$ is just used to denote the $n$-th closest inner neighbour to the point at $x$. This boundary condition produces good enough results when evolving the BSSN system, but if one adds a scalar field to it, with a wave-like evolution equation, there is production of undesirable ingoing modes that spoil the evolution.

The second option, and the one used throughout the numerical simulations in this work, is the Sommerfeld boundary condition, also known as radiation condition. It is common practice in Numerical Relativity – and other fields where Method of Lines evolutions are performed – to employ this sort of boundary condition, where the aim is to have the evolved functions act as waves that go through the boundary with minimal reflections.

To derive this boundary condition, we will assume spherical coordinates. Let us start by considering

the wave equation,

$$\frac{1}{v^2}\partial_t^2 u = \nabla^2 u, \tag{3.47}$$

where $u \equiv u(t, r, \theta, \varphi)$ is some function of time and space. Furthermore, let us assume $u$ is spherically symmetric, so that all dependences in $\theta$ and $\varphi$ in equation (3.47) vanish. The wave equation is thus simplified to [3]

$$\frac{1}{v^2}\partial_t^2 u = \partial_r^2 u + \frac{2}{r}\partial_r u. \tag{3.48}$$

The general solution to this equation is of the form

$$u(r, t) = A\frac{u(r + vt)}{r} + B\frac{u(r - vt)}{r}, \tag{3.49}$$

which has the physical interpretation of a superposition of an ingoing and an outgoing wave.

With this solution to the wave equation, we now intend to make our grid functions $f$ behave like outgoing, spherically symmetric waves at the boundaries. This can be achieved by making the ansatz

$$f = f_0 + \frac{u(r - vt)}{r} + \frac{c}{r^n}, \tag{3.50}$$

where $f_0$ is an asymptotic value for $f$, and $c/r^n$ is a radial falloff term that acts as a correction for incoming waves and other undesirable behaviour. It is useful, however, to transform condition (3.50) into a condition for the time derivative of $f$, because then one would be able to evolve the points at the outer boundaries in the same way as all the other points, by using the Method of Lines. Differentiating the previous equation with respect to time, we obtain

$$\partial_t f = -v\frac{u'(r - vt)}{r}. \tag{3.51}$$

Taking now a derivative of equation (3.50) with respect to $r$, we get

$$\partial_r f = \frac{u'(r - vt)}{r} - \frac{u(r - vt)}{r^2} - \frac{nc}{r^{n+1}}. \tag{3.52}$$

Solving (3.52) to obtain $u'(r - vt)/r$ and plugging into (3.51) results in

$$\partial_t f = -v\left[\partial_r f + \frac{u(r - vt)}{r^2} + \frac{nc}{r^{n+1}}\right]. \tag{3.53}$$

The term $u(r - vt)/r^2$ on the right-hand side of (3.53) can be cancelled out by plugging in the ansatz (3.50). Defining $k = -vc(n - 1)$, we obtain the final form of the Sommerfeld boundary condition,

$$\partial_t f = -\frac{v}{r}\left[r\partial_r f + (f - f_0) + \frac{k}{r^{n+1}}\right]. \tag{3.54}$$

This boundary condition can be applied in any curvilinear coordinate system, with coordinates $(x^i)$,

[3] The right-hand side of equation (3.48) is simply the radially-dependent part of the Laplacian in spherical coordinates, which can be derived in a number of ways.

by taking $r \equiv r\left(x^i\right)$. The radial derivative in the evolution equation above becomes

$$\partial_r f = \frac{\partial x^i}{\partial_r} \partial_i f. \tag{3.55}$$

It might be impossible to invert the relation $r\left(x^i\right)$ to compute the right-hand side of (3.55), but this can be achieved also by computing the Jacobian matrix,

$$J^j_i = \frac{\partial x^j_{\text{Sph}}\left(x^i\right)}{x^i}, \tag{3.56}$$

where $x^j_{\text{Sph}} = (r, \theta, \varphi)$ are the spherical coordinates, and invert $J^j_i$, obtaining

$$\left(J^j_i\right)^{-1} = \frac{\partial x^i}{\partial x^j_{\text{Sph}}}, \tag{3.57}$$

which can be used directly in (3.55).

With this overview of the implementation of boundary conditions within NRPy+, we conclude our presentation of the main features of this code generation tool. In the next chapter we will use NRPy+ to evolve scalar fields in black hole spacetimes.

# Chapter 4

# Numerical evolutions: initial data, implementation and results

In Chapter 1 of this work, we went through the history of gravitational physics, with a focus on General Relativity. Next, in Chapter 2 laid out the 3+1 Formalism of Numerical Relativity, as well as the BSSN evolution scheme, which intend to provide a framework to evolve the Einstein equations (1.2) numerically. Finally, in Chapter 3 we iterated on the BSSN equations, making them covariant and rescaling the vector and tensor variables therein, allowing for numerical evolution in general curvilinear coordinate systems.

At the end of the previous chapter, we also presented NRPy+ [34], a set of libraries, written in Python, that aim to generate optimised C code that can be used to evolve spacetimes in General Relativity. Now, we have at our disposal all the tools needed to do numerical simulations of physically interesting spacetimes. This is the aim of this chapter and, in a broader sense, of this thesis.

## 4.1 Initial data for a rotating black hole

Initial data is one the most important parts of any numerical solution of a Cauchy problem. It establishes the physical situation one wants to study over time. In section 3.3.3 we listed some of the available initial data modules within NRPy+, as well as the specific workings of the code that allow for the translation of symbolic expressions and numerical data to C variables. In this section, we will study in some detail the UIUC Black Hole initial data [52], which will be used as the background spacetime for all the evolutions throughout this thesis.

As mentioned several times up to this point, the presence of singularities in a spacetime spoils numerical evolution very quickly. These singularities may present themselves as coordinate singularities, like the event horizon at $r_S = 2M$ in the Schwarzschild solution (1.3). However, the spacetime can also have physical singularities, which is what happens at the centre of a black hole. Coordinate singularities can be obviously dealt with by finding a non-singular coordinate system, but if the spacetime is singular, other techniques must be employed.

Historically, there are two main ways to deal with the black hole singularities. The first is called

*excision* and, as the name indicates, it consists of manually removing the interior of a black hole from the numerical domain, thus getting rid of the singularity at the centre. This was suggested in 1984 by Unruh, as cited by Thornburg [56]. The downside of this method is that an *apparent horizon*[1] must be found at every time slice, so that its interior can be removed from the domain. Apparent horizon finders solve elliptic equations that increase the computational strain for each time step, potentially slowing down the evolution in a significant way.

The second, and most common, way to deal with black hole singularities is known as *puncture* techniques. The name comes from the fact that, in this paradigm, each slice $\Sigma$ of constant coordinate time $t$ corresponds to $\mathbb{R}^3$, except for a set of points, each corresponding to a singularity. These techniques are further subdivided into *static punctures*, where the positions of the singularities are kept constant and the divergent behaviour of grid quantities is analytically separated from the regular parts [57], and *moving punctures*, where, through a singularity avoiding gauge choice, the physical singularity does not present itself in the computational domain, making the punctures correspond to coordinate singularities [58, 59]. Here, we shall be interested in evolving a single black hole, through the use of initial data built under the moving puncture paradigm.

The UIUC Black Hole initial data was introduced in 2010 by Liu *et al.* [52], with the aim of surpassing the extremal Bowen-York limit [60] for the spin of a Kerr black hole in numerical evolution. Until that point, conformally flat puncture initial data could only be accurately evolved if the black hole's dimensionless spin $\chi \equiv a/M$ obeyed $\chi \lesssim 0.93$, while the Kerr limit corresponds to $\chi < 1$. This results in an inability to probe potentially interesting physics around very rapidly rotating black holes.

Spinning black holes with zero electric charge are represented by the Kerr metric,

$$\mathrm{d}s^2 = -\left(1 - \frac{2Mr_{\mathsf{BL}}}{\Sigma}\right)\mathrm{d}t^2 - \frac{4aMr_{\mathsf{BL}}\sin^2\theta}{\Sigma}\mathrm{d}t\mathrm{d}\varphi + \frac{\Sigma}{\Delta}\mathrm{d}r_{\mathsf{BL}}^2 + \Sigma\mathrm{d}\theta^2 + \frac{A}{\Sigma}\sin^2\theta\mathrm{d}\varphi^2, \tag{4.1}$$

which corresponds to the line element (1.4) when $Q = 0$. Here we define the variables $\Delta$, $\Sigma$ and $A$ as

$$\Delta = r_{\mathsf{BL}}^2 - 2Mr_{\mathsf{BL}} + a^2, \tag{4.2a}$$

$$\Sigma = r_{\mathsf{BL}}^2 + a^2\cos^2\theta, \tag{4.2b}$$

$$A = \left(r_{\mathsf{BL}}^2 + a^2\right) - \Delta a^2\sin^2\theta, \tag{4.2c}$$

$a$ is the spin per unit mass, as in equation (1.5c), $M$ is the black hole mass, and $r_{\mathsf{BL}}$ is the Boyer-Lindquist radial coordinate.

Proceeding to a 3+1 decomposition of the Kerr metric, the spatial 3-metric can be easily read from the line element above. It takes the form

$$\mathrm{d}l^2 = \frac{\Sigma}{\Delta}\mathrm{d}r_{\mathsf{BL}}^2 + \Sigma\mathrm{d}\theta^2 + \frac{A}{\Sigma}\sin^2\theta\mathrm{d}\varphi^2. \tag{4.3}$$

[1] An event horizon is defined as the boundary of the causal past of future null infinity. Therefore, its existence is a global property of a spacetime, and thus cannot be determined locally on each hypersurface $\Sigma$ of constant coordinate time $t$. An apparent horizon, however, is a local 2 dimensional surface that can be determined for each $t$. Furthermore, if it exists, it can be shown to always be inside an event horizon. Therefore, in most numerical simulations, one searches for apparent horizons at runtime instead of an event horizon in post-processing.

The shift vector $\beta_i$ that keeps the spacetime stationary can also be read from the off-diagonal elements of (4.1). Contracting with the inverse spatial metric $\gamma^{ij}$ to raise the covariant index, one gets

$$\beta^i = \left(0, 0, -\frac{2Mar_{\mathsf{BL}}}{A}\right). \tag{4.4}$$

The lapse can be determined by equation (5.49) of reference [27],

$$g_{00} \equiv g_{tt} = -\alpha^2 + \beta_k \beta^k, \tag{4.5}$$

which, in this particular case, gives

$$\alpha^2 = \frac{4M^2 r_{\mathsf{BL}}^2 a^2 \sin^2\theta}{\Sigma A} - \frac{a^2 \sin^2\theta - \Delta}{\Sigma}. \tag{4.6}$$

After a lengthy computation, it is possible to show that

$$\alpha = \sqrt{\frac{\Delta\Sigma}{A}}. \tag{4.7}$$

It is important to note, however, that $\alpha$ and $\beta^i$ are gauge choices, so they can be chosen to have different values from the above. These expressions correspond to the gauge choice that results in a stationary metric, even though that may not be the most advantageous choice in the context of numerical evolution.

The Kerr solution to Einstein's equations is characterised by two horizons at $r_{\mathsf{BL}} = r_+, r_-$, with

$$r_\pm = M \pm \sqrt{M^2 - a^2}. \tag{4.8}$$

At these points, the Boyer-Lindquist coordinates are singular. As suggested by Brandt and Seidel [61], it is possible to resolve this issue by introducing a new, dimensionless radial coordinate $\eta$, defined implicitly through

$$r = r_+ \cosh^2\left(\frac{\eta}{2}\right) - r_- \sinh^2\left(\frac{\eta}{2}\right). \tag{4.9}$$

With this choice, the event horizon at $r_+$ is mapped to $\eta = 0$. Furthermore, the radial coordinate range is $\eta \in (-\infty, +\infty)$, where both positive and negative values of $\eta$ correspond to $r_{\mathsf{BL}} \in [r_+, +\infty)$. Therefore, the 3-metric written in these coordinates,

$$\mathrm{d}l^2 = \Psi_0^4 \left[e^{-2q_0}\left(\mathrm{d}\eta^2 + \mathrm{d}\theta^2\right) + \sin^2\theta \mathrm{d}\varphi^2\right], \tag{4.10}$$

where

$$\Psi_0^4 = \frac{A}{\Sigma} \quad \text{and} \quad e^{-2q_0} = \frac{\Sigma^2}{A} \tag{4.11}$$

corresponds to a wormhole geometry, where two asymptotically flat universes are connected through an Einstein-Rosen bridge at the throat $\eta = 0$.

Brandt and Seidel [61] propose the definition, from $\eta$, of a quasi-isotropic radial coordinate, *i.e.* a radial coordinate $\bar{r}$ that is reduced to the Schwarzschild isotropic coordinates when $a \to 0$. However, in

this coordinate, the position of the event horizon goes to zero when $\chi \to 1$, which impedes the evolution of extremal black hole spacetimes. Liu *et al.* [52] generalise their proposal by suggesting a radial coordinate of the form

$$r = \frac{\sqrt{M^2 - a^2}}{2} \lambda\left(a, \eta\right) e^{\eta}. \tag{4.12}$$

The function $\lambda\left(a, \eta\right)$ is, in principle, arbitrary. With the choice

$$\lambda = \frac{e^{-\eta}}{\sqrt{M^2 - a^2}} \left[ r_{\mathsf{BL}} - \frac{r_+}{2} + \sqrt{r_{\mathsf{BL}}\left(r_+ - r_-\right)} \sinh\left(\frac{\eta}{2}\right) \right] \tag{4.13}$$

we obtain a quasi-isotropic $r$ coordinate that relates to the Boyer-Lindquist radial coordinate through

$$r_{\mathsf{BL}} = r \left(1 + \frac{r_+}{4r}\right)^2. \tag{4.14}$$

This coordinate results in a non-zero position for the event horizon, irrespective of black hole spin. It also coincides with $r_{\mathsf{BL}}$ at spatial infinity. In these new coordinates, the event horizon is located at

$$r_h = \frac{r_+}{4}. \tag{4.15}$$

The spatial metric reads

$$\mathrm{d}l^2 = \frac{\Sigma\left(r + \frac{r_+}{4}\right)^2}{r^3\left(r_{\mathsf{BL}} - r_-\right)} \mathrm{d}r^2 + \Sigma \mathrm{d}\theta^2 + \frac{A \sin^2\theta}{\Sigma} \mathrm{d}\varphi^2. \tag{4.16}$$

In order to construct initial data for the Kerr spacetime, in any coordinate system, one also needs to know the extrinsic curvature $K_{ij}$. Its only non-zero components with this quasi-isotropic radial coordinate are

$$K_{r\varphi} = K_{\varphi r} = \frac{Ma \sin^2\theta}{\Sigma\sqrt{A\Sigma}} \left[3r_{\mathsf{BL}}^4 + 2a^2 r_{\mathsf{BL}}^2 - a^4 - a^2\left(r_{\mathsf{BL}}^2 - a^2\right)\sin^2\theta\right] \left(1 + \frac{r_+}{4r}\right) \frac{1}{\sqrt{r\left(r_{\mathsf{BL}} - r_-\right)}}, \tag{4.17a}$$

$$K_{\theta\varphi} = K_{\varphi\theta} = -\frac{2a^3 M r_{\mathsf{BL}} \cos\theta \sin^3\theta}{\Sigma\sqrt{A\Sigma}} \left(r - \frac{r_+}{4}\right) \sqrt{\frac{r_{\mathsf{BL}} - r_-}{r}}. \tag{4.17b}$$

By introducing the quasi-isotropic radial coordinate, we took the wormhole geometry of the line element (4.10) and compactified the universe corresponding to $\eta \in (-\infty, 0]$ to the range $r \in (0, r_h]$, whilst the other side of the throat at the horizon now corresponds to $r \in [r_h, +\infty)$. Therefore, in these coordinates, the origin at $r = 0$ is a coordinate singularity, corresponding to the asymptotically flat spatial infinity of one of the two universes. The physical singularity at the centre of the black hole is completely avoided by this choice of coordinates.

## 4.2 Convergence testing for black hole evolutions

When dealing with Method of Lines simulations, one discretises the continuous computational domain into a set of grid points, wherein the evolved grid functions are to be evaluated at each coordinate time slice $\Sigma_t$. As mentioned in section 3.3.4, since the evolution equations within our covariant BSSN scheme involve the computation of spatial derivatives, one has to resort to techniques, such as finite differences,

to approximate the continuous differential operators on our discrete grid. By doing so, the numerical accuracy of the solution becomes limited by the accuracy of these approximations.

Consider a PDE of the form

$$\partial_t u = Pu, \tag{4.18}$$

where $u \equiv u(t,x)$ is a function of time $t$ and a single space variable $x$, and $P$ is a general linear differential operator where no derivatives with respect to time appear. As we have seen, this operator $P$ can be approximated via finite differences by an operator $Q$, whose expression is obtained by the Taylor series expansion of $u$ at the grid points, as described in section 3.3.4. This approximation is accurate up to order $N_{\text{FD}}$, by Taylor's theorem. What this means is that, under the context of a MoL evolution of equation (4.18), for a given time $t$, the difference between the solution $u$ and its numerical approximation $u_{\text{num}}$ obeys the relation

$$\|u(t,x) - u_{\text{num}}(t,x)\| \leq K(\Delta x)^{N_{\text{FD}}}, \tag{4.19}$$

where $\Delta x$ is the uniform spacing between grid points, and $\|\cdot\|$ is a suitable norm. This relation is valid as long as $u(x,t)$ is smooth and the time evolution is stable, *i.e.* it satisfies relation (2.23) for all time.

Relation (4.19) is very useful to study the convergence of a numerical method to its real solution. In general, the truncation errors from the finite difference approximations performed to compute the right-hand side of the evolution equations will be the dominant source of inaccuracy in the numerical evolution. Thus, by evolving the same code with varying values of $\Delta x$ – or, equivalently, varying number of grid points $N$ – in a given direction, one can check if this behaviour is evident.

In the context of BSSN evolutions, a particularly useful quantity to look for convergence with is the Hamiltonian constraint violation $\mathcal{H}$, as its value for any solution that obeys the Einstein equations is $\mathcal{H} = 0$ for all $t$ and in every point of the domain.[2] For $\mathcal{H}$, equation (4.19) is equivalent to

$$|\mathcal{H}_{\text{num}}| = \frac{\kappa}{N^{N_{\text{FD}}}}, \tag{4.20}$$

where we wrote $\Delta x \propto N^{-1}$, with $N$ being the number of points in the $x$ direction, and absorbed all multiplicative constants into $\kappa$. The factor $\kappa$ is of order unity, and it depends on the finite differencing method used, but not on $N$. By taking two different grid resolutions, say $N_1$ and $N_2$, taking relation (4.20) for each of those grids and dividing them together yields

$$\frac{|\mathcal{H}_1|}{|\mathcal{H}_2|} = \left(\frac{N_2}{N_1}\right)^{N_{\text{FD}}}. \tag{4.21}$$

Using the equation above, we can probe the rate of convergence of simulations using NRPy+. To that end, using the UIUC Black Hole initial data described in section 4.1 above, several simulations of a Schwarzschild wormhole spacetime (obtained by setting $\chi = 0$) with mass $M = 1$ were performed, with varying radial resolution. The boundary of the computational domain was set at $R_{\text{max}}/M = 20$ and the spacetime was allowed to evolve until the coordinate time reached $t/M = R_{\text{max}}$. The right-hand side of

[2] This characteristic is obviously shared with the momentum constraints $\mathcal{M}^i$, as they must also be obeyed in a numerical evolution of the BSSN equations.

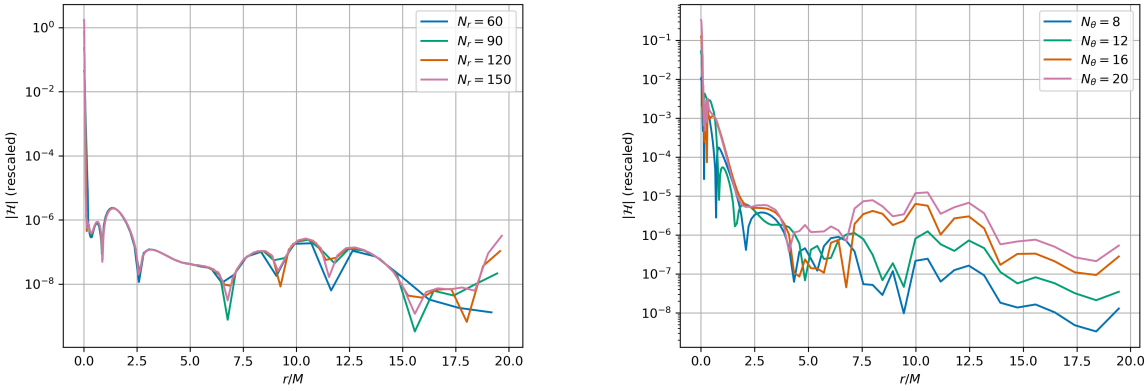


(a) $\chi = 0$ (b) $\chi = 0.99$

Figure 4.1: Convergence tests for the evolution of a single black hole using UIUC initial data, for the non-spinning and extremal spin cases. The plots correspond to the coordinate time slice $t/M \approx 10$. For the non-spinning case (a), $N_\theta = 8$ and $N_\varphi = 16$, while for the rapidly spinning case (b), $N_r = 90$ and $N_\varphi = 16$.

the evolutions equations employed 4$^{\text{th}}$ order finite difference methods for the spatial derivative operators. On the left panel of Figure 4.1 we plot the absolute value of the Hamiltonian constraint violation as a function of $r$ for $t/M \approx 10$, for a line of constant $\theta$ and $\varphi$. The values for $|\mathcal{H}|$ for the higher radial resolutions, namely for $N_r > N_{\text{ref}} \equiv 60$, were rescaled, as the axis label indicates, by multiplication of the values at each grid point by the factor at the right-hand side of equation (4.21), where $N_1$ and $N_2$ are taken to be $N_r$ and $N_{\text{ref}}$, respectively. This rescaling should approximately match the plots for each resolution to that of the lowest $N_r$, as long as the truncation error is the dominant source of numerical inaccuracy. As is shown in the Figure, this is almost exactly what happens for $r/M \lesssim 6.5$. After that point, the propagation of error from the approximate boundary conditions dominates, but even then there is a remarkable superposition of the plots.[3]

Since, in this work, we also aim to study rapidly spinning black hole spacetimes, a similar study of the convergence behaviour was performed with a near-extremal spinning black hole, with dimensionless spin $\chi = 0.99$, with all other parameters unchanged when compared to the non-spinning case above. This testing revealed that the expected convergence behaviour was not apparent when varying the number of points in the radial direction. However, the obvious reason for this phenomenon is that, as the spin increases, the spacetime deviates further from a spherically symmetric configuration, and the variation in $\theta$ becomes very important. Therefore, on the right side of Figure 4.1 we show the Hamiltonian constraint violation for the rapidly spinning spacetime, with varying $N_\theta$. The same rescaling procedure was employed, with the rescaling coefficient being computed with the number of points in the $\theta$ direction for each case. Compared to the Schwarzschild case, this plot looks quite a bit messier. However, the same general characteristics are evident: up to $r/M \lesssim 6.5$ the curves are on the same order of magnitude, even though they to not coincide completely; after this point, as before, the propagation of

[3] In these simulations, the radial coordinate is of the type *SinhSpherical*, with $r$ given by equation (3.27) and $w_s = 0.2$. Therefore, there is a smaller density of grid points near the boundary at $r = R_{\text{max}}$, and the numerical error from the boundary penetrates the domain much faster. However, as the error encounters the region with larger density of grid points, the propagation is slower, making sure it doesn't reach the most physically interesting region near the origin.

numerical error from the boundary dominates, and the plots stray further from each other.

For both the cases above, it is important to note a few things. Firstly, the order of magnitude of the Hamiltonian constraint violation is quite small in most of the computational domain. It is also on par with the results of Ruchlin et al. [34], where NRPy+ was presented and also compared to other codes, like the Einstein Toolkit [33], showing general agreement between the two. This helps validate the proposition of using NRPy+ to generate code that is capable of numerical simulation of spacetimes in General Relativity with numerical accuracy that is at least as good as other popular tools in Numerical Relativity.

Secondly, in both plots of Figure 4.1 we see a significant spike of the Hamiltonian constraint violation to values close to order unity for $r \to 0$. The reason for this is clear if we remember that the quasi-isotropic slices of Kerr spacetime we are evolving have a wormhole geometry. This means that the region near the origin represents a whole asymptotically flat region of spacetime equivalent to the rest of the computational domain. Obviously covering this region with only a small number of grid points results in large numerical inaccuracy. However, this is not a problem as the presence of an event horizon prevents the propagation of information from this region to our region of interest, $r > r_h$, which is evident from the fact that we are able to achieve convergence of the $\mathcal{H}$ to zero at the expected rate.

Also noteworthy is the fact that the simulations presented here were performed on a desktop computer using a 16 thread processor, taking anywhere from a couple of minutes to a couple of hours to run, depending on the grid resolution. This is remarkable performance when compared, again, to codes like the Einstein Toolkit that, while very robust, are very computationally expensive due to the use of Cartesian coordinates with complex AMR algorithms.

## 4.3 Scalar field: equations of motion and initial data

We now wish to take the black hole spacetimes evolved in the previous section and add fundamental fields to them. In particular, we'd like to study how scalar fields evolve in these curved geometries. This can be done by coupling the Klein-Gordon equation,

$$\left(\nabla^{\mu}\nabla_{\mu} - \mu_S^2\right)\Phi - V'\left(\Phi\right) = 0, \tag{4.22}$$

to the Einstein field equations (1.2) of General Relativity. Here, $V'\left(\Phi\right)$ is a self-interaction potential for the field which, for the purposes of this work, will always be set to zero, and $\mu_S$ is the mass coupling of the field. The Klein-Gordon equation determines the evolution of the scalar field $\Phi$, which in turn is responsible for a backreaction onto the metric $g_{\mu\nu}$, by means of a non-zero stress-energy tensor $T_{\mu\nu}$, given by

$$T_{\mu\nu} = -\frac{1}{2}g_{\mu\nu}\left(\partial_{\alpha}\Phi^{*}\partial^{\alpha}\Phi + \mu_S^2\Phi^{*}\Phi\right) + \frac{1}{2}\left(\partial_{\mu}\Phi^{*}\partial_{\nu}\Phi + \partial_{\mu}\Phi\partial_{\nu}\Phi^{*}\right), \tag{4.23}$$

that acts as a source term for the geometry.

However, to be able to include the evolution of the scalar field in our Numerical Relativity framework, we must proceed to the 3+1 decomposition of its equation of motion (4.22) and the corresponding stress-

energy tensor source terms for the BSSN equations. To do so, following the treatment of Okawa *et al.* [62], let us first define a new field variable $\Pi$, by

$$(\partial_t - \mathcal{L}_\beta)\,\Phi = -\alpha\Pi. \tag{4.24}$$

This variable is the field analogous to the extrinsic curvature $K_{ij}$, which can be physically interpreted as a time derivative of the spatial metric $\gamma_{ij}$ by equation (2.18). Furthermore, the definition above is also seen as the evolution equation of $\Phi$ in our decomposition, thus making the system of equations first order in time. A 3+1 decomposition of the Klein-Gordon equation (4.22) yields

$$(\partial_t - \mathcal{L}_\beta)\,\Pi = \alpha\left(-D^i D_i\Phi + K\Pi + \mu_S^2\Phi\right) - D^i\alpha D_i\Phi, \tag{4.25}$$

with $D_i$ being the covariant derivative associated with the physical spatial metric $\gamma_{ij}$. Expanding the covariant derivatives and Lie derivatives in Equations (4.24) and (4.25), we get the evolution equations for the fields,

$$\partial_t\Phi = -\alpha\Pi + \beta^i\partial_i\Phi, \tag{4.26a}$$

$$\partial_t\Pi = \alpha(-\gamma^{ij}\partial_j\partial_i\Phi + \gamma^{ij}\Gamma^k_{ji}\partial_k\Phi + K\Pi + \mu_s^2\Phi) - \gamma^{ij}\partial_j\alpha\partial_i\Phi + \beta^i\partial_i\Phi. \tag{4.26b}$$

If one wishes to minimally couple[4] a scalar field $\Phi$ to General Relativity, it is necessary to obtain the source terms for the 3+1 Einstein equations (2.21). The energy density $\rho$, defined in equation (2.9), reads

$$\rho = \frac{1}{2}\left(\Pi^*\Pi + \mu_S^2\Phi^*\Phi + D_k\Phi^* D^k\Phi\right). \tag{4.27a}$$

The momentum density $S_i$, as in equation (2.11), gives

$$S_i = \frac{1}{2}\left(\Pi D_i\Phi^* + \Pi^* D_i\Phi\right). \tag{4.27b}$$

Finally, the spatial stress tensor, defined by equation (2.16), is given by

$$S_{ij} = \frac{1}{2}\gamma_{ij}\left(\Pi^*\Pi - \mu_S^2\Phi^*\Phi - D^k\Phi^* D_k\Phi\right) + \frac{1}{2}\left(D_i\Phi^* D_j\Phi + D_i\Phi D_j\Phi^*\right). \tag{4.27c}$$

The evolution equations above are written in terms of the ADM quantities. However, to be consistent with the formalism developed in previous chapters, one should write these equations in terms of BSSN quantities, like the conformally related spatial metric $\bar{\gamma}_{ij}$. Doing so, the evolution equation for $\Phi$ remains unchanged, while the one for $\Pi$ reads

$$\partial_t\Pi = \alpha\left(-e^{-4\phi}\bar{\gamma}^{ij}\partial_i\partial_j\Phi + e^{-4\phi}\bar{\gamma}^{ij}\bar{\Gamma}^k_{ij}\partial_k\Phi - 2e^{-4\phi}\bar{\gamma}^{ij}\partial_j\Phi\partial_i\phi + K\Pi + \mu_s^2\Phi\right) - e^{-4\phi}\bar{\gamma}^{ij}\partial_j\alpha\partial_i\Phi + \beta^i\partial_i\Pi. \tag{4.28}$$

The next issue to solve is that of physically meaningful initial data for the scalar field variables $\Phi$ and $\Pi$. Since we intend to solve the coupled Einstein-Klein-Gordon system, it is of utmost importance that

[4] By minimally couple it is meant that the self-interaction potential $V'$ in equation (4.22) is 0, and the coupling is done through the stress-energy tensor exclusively.

our initial data satisfy the constraint equations, at least partially[5]. In reference [62], Okawa *et al.* show that, for a Schwarzschild spacetime in isotropic coordinates, one can take the ansatz

$$\Pi = \frac{\psi^{-5/2}}{\sqrt{r\pi}} F(r) Z(\theta, \varphi), \tag{4.29a}$$

$$\psi = \psi_S + \sum_{l,m} \frac{u_{lm}(r)}{r} Y_{lm}(\theta, \varphi), \tag{4.29b}$$

where

$$\psi_S = 1 + \frac{M}{2r} \tag{4.30}$$

is the conformal factor one obtains by performing a conformally flat decomposition of the Schwarzschild metric in isotropic coordinates, $r$ is the isotropic radial coordinate, $Y_{lm}$ are spherical harmonics and $u_{lm}(r)$, $F(r)$ and $Z(\theta, \varphi)$ are undetermined functions. Furthermore imposing the maximal slicing condition, $K = 0$, and $\Phi = 0$ at the initial time instant, the constraints reduce to ordinary differential equations involving $u_{lm}$, $F$ and $Z$, which read

$$\sum_{lm} \left( u''_{lm} - \frac{l(l+1)}{r^2} u_{lm} \right) Y_{lm} = -F^2(r) Z^2(\theta, \varphi). \tag{4.31}$$

In reference [62], two sets of analytical initial data that solve equation (4.31) are given: a spherically symmetric one, and a dipole configuration for the field. For the former, the functions $F$ and $Z$ are given by

$$F(r) = A_{00} \sqrt{r} e^{-\frac{(r-r_0)^2}{w^2}} \tag{4.32a}$$

and

$$Z(\theta, \varphi) = \frac{1}{\sqrt{4\pi}}. \tag{4.32b}$$

The only non-zero component of $u_{lm}$ that satisfies equation (4.31) is that with $l = m = 0$, which reads

$$u_{00} = A_{00}^2 \frac{w\left[w^2 - 4r_0(r - r_0)\right]}{16\sqrt{2}} \left\{ \operatorname{erf}\left[ \frac{\sqrt{2}(r - r_0)}{w} \right] - 1 \right\} - A_{00}^2 \frac{r_0 w^2}{8\sqrt{\pi}} e^{\frac{-2(r-r_0)^2}{w^2}} \tag{4.33}$$

The dipole type of initial data, on the other hand, can be achieved by setting the functions $F$ and $Z$ to

$$F(r) = A_{11} r e^{-\frac{(r-r_0)^2}{w^2}} \tag{4.34a}$$

and

$$Z(\theta, \varphi) = Y_{1-1} - Y_{11} = \sqrt{\frac{3}{2\pi}} \sin\theta \cos\varphi, \tag{4.34b}$$

with $A_{11}$ being the scalar field amplitude, and $r_0$ and $w$ the gaussian centre and width, respectively. For

[5] We shall say that the constraints are partially satisfied if the values of the constraint violation are small enough as to not dominate the error of the simulations.

these, it can be shown that the non-vanishing $u_{lm}$ that adhere to equation (4.31) are

$$\begin{aligned} u_{22} = u_{2-2} = &- \frac{A_{11}^2 w^2}{80 r^2}\sqrt{\frac{3}{10\pi}} e^{-\frac{2(r-r_0)^2}{w^2}} \left[4\left(r^4 + r^3 r_0 + r^2 r_0^2 + r r_0^3 + r_0^4\right) + w^2\left(4r^2 7 r r_0 + 9 r_0^2\right) + 2w^4\right] \\ &+ A_{11}^2 \sqrt{\frac{3}{5}} \frac{w\left(-16r^5 + 16 r_0^5 + 40 r_0^3 w^2 + 15 r_0 w^4\right)}{320 r^2} \left\{\operatorname{erf}\left[\frac{\sqrt{2}\,(r-r_0)}{w}\right] - 1\right\} \\ &+ A_{11}^2 \sqrt{\frac{3}{5}} \frac{w r_0\left(16 r_0^4 + 40 r_0^2 w^2 + 15 w^4\right)}{320 r^2} \left[\operatorname{erf}\left(\frac{\sqrt{2} r_0}{w}\right) + 1\right] \\ &+ A_{11}^2 \sqrt{\frac{6}{5\pi}} e^{-\frac{2r_0^2}{w^2}} \frac{2w^2\left(4 r_0^4 + 9 r_0^2 w^2 + 2 w^4\right)}{320 r^2}, \end{aligned} \tag{4.35a}$$

$$u_{20} = -\sqrt{\frac{2}{3}} u_{22}, \tag{4.35b}$$

$$u_{00} = \frac{A_{11}^2 w}{16}\left\{-\frac{2w\left(2r_0^2 + w^2\right) e^{-\frac{2(r-r_0)^2}{w^2}}}{\sqrt{\pi}} - \sqrt{2}\left[4\left(r - r_0\right) r_0^2 + \left(r - 3r_0\right) w^2\right]\left[\operatorname{erf}\left(\frac{\sqrt{2}\,(r-r_0)}{w} - 1\right)\right]\right\}. \tag{4.35c}$$

In the reference, initial data for the scalar field in a Kerr spacetime, using the quasi-isotropic coordinates of section 4.1, are also detailed. However, these are not defined by closed-form expressions, but rather by the numerical solution of an elliptic equation. Finally, the authors also set up initial data for pseudo-bound states, which are ideal to study superradiant instabilities of massive fields in black hole geometries. Conversely, the states detailed above are more advantageous in the case of scattering experiments.

For the purpose of creating long-lived, pseudo-bound states, where the scalar field forms a cloud around the black hole that remains present for large time scales, we set up a simplified version of the pseudo-bound initial data provided by Okawa *et al.* [62]. In their work, the authors assume a complex scalar field, which is given by the ansatz

$$\Phi\left(t, r, \theta, \varphi\right) = \frac{A_P}{\sqrt{\pi}} \exp\left[i\left(\omega t + m\varphi\right) - \frac{\left(r - r_0\right)^2}{w^2}\right] Z\left(\theta\right). \tag{4.36}$$

Here, $r_0$ and $w$ are the usual Gaussian profile centre and width, respectively, $A_P$ is the amplitude of the profile, $\omega$ is a frequency, $m$ is an integer, and $Z\left(\theta\right)$ is some function that provides a dependence on $\theta$. From the definition of $\Pi$ we can obtain its expression for these initial data, which reads

$$\Pi\left(t, r, \theta, \varphi\right) = \frac{i}{\alpha}\left(m\beta^{\varphi} - \omega\right)\Phi, \tag{4.37}$$

where $\beta^{\varphi}$ is the only non-zero component of the shift for the rotating black hole initial data described in section 4.1, as indicated in equation (4.4).

In the reference, the authors proceed to solve the Hamiltonian and momentum constraints, as one should in order to provide initial data describing a real physical situation. This leads them, much like in the case for scattering initial data in a Kerr background, to an elliptic PDE for a correction to the conformal factor that must be solved numerically. However, due to time constraints, a simplified constraint-violating

set of initial data was implemented. These data can be obtained from Equations (4.36) and (4.37) above by imposing that $\Phi$ be real and, furthermore, that $Z(\theta) = \sin\theta$. Taking the real part of (4.36), we obtain

$$\Phi(t, r, \theta, \varphi) = \frac{A_P}{\sqrt{\pi}} e^{\frac{-(r-r_0)^2}{w^2}} \cos(\omega t + m\varphi) \sin\theta. \tag{4.38}$$

We can compute the expression for $\Pi$ from the definition (4.24) and, again, taking $\beta^i$ given by the expression (4.4). This yields

$$\Pi = \frac{A_P}{\alpha\sqrt{\pi}} e^{\frac{-(r-r_0)^2}{w^2}} (m\beta^\varphi - \omega) \sin(\omega t + m\varphi) \sin\theta. \tag{4.39}$$

As we shall see below, these initial data lead to results that are qualitatively similar to those presented in [62], *i.e.* long-lived scalar clouds around black holes can be developed and maintained.

### 4.3.1 Implementation and convergence testing

To implement the evolution equations and initial data into the infrastructure of NRPy+ and, with it, generate C code that allows for the evolution of the coupled Einstein-Klein-Gordon system of equations, four new modules were written and added to the base code. These are as follows:

- `ScalarFieldRHSs` – registers the grid functions for $\Phi$ and $\Pi$, the scalar field variables, and defines the right-hand side expressions of the evolution equations (4.26a) and (4.28) for these quantities;
- `ScalarFieldT4munu` – defines the expressions for the source terms $\rho$, $S_i$ and $S_{ij}$ of Equations (4.27), as well as the derived quantities that appear in the evolution equations of the covariant BSSN formulation (3.7) and that should be added to the vacuum expressions that are generated by the standard NRPy+ modules;
- `ScalarFieldID` – defines the expressions for several types of initial data for the scalar field variables, including the constraint satisfying and simplified pseudo-bound initial data described above;
- `ScalarField_ID_function_string` – takes the symbolic expressions for the initial data defined in `ScalarFieldID` and uses them to generate C code that implements these data.

The modules listed above can then be used, in conjunction with other NRPy+ modules, namely the ones that generate the right-hand side expressions of the covariant BSSN equations as well as the aforementioned UIUC Black Hole initial data module of section 4.1, to generate optimised C code that evolves the system forward in time.

To validate the implementation of the constraint satisfying initial data, in both the spherically symmetric and dipolar configurations, convergence tests were performed. To do so, we proceeded in a way that is similar to what was described in section 4.2, where convergence tests were performed on the metric without the presence of matter fields. Specifically, we set up initial data with the parameters listed in Table 4.1 for four different radial resolutions, computed the Hamiltonian constraint violation using equation (2.34f) with the spatial derivatives replaced by the corresponding fourth-order finite difference operators,

| Parameter | Gaussian | Dipole |
|---|---|---|
| $N_\theta$ | 8 | 16 |
| $N_\varphi$ | 16 | 32 |
| $M$ | 1.0 | 1.0 |
| $A$ | 0.075 | 0.075 |
| $r_0$ | 5.0 | 5.0 |
| $w$ | 0.5 | 0.5 |
| $\mu_S$ | 0.0 | 0.0 |
| $R_{\text{max}}$ | 20.0 | 20.0 |

Table 4.1: Parameters used for the convergence tests of the constraint-satisfying scalar field initial data for both Gaussian and dipolar configurations. The results for these tests are shown in Figure 4.2. The parameter $A$ corresponds to the amplitude $A_{00}$ or $A_{11}$, depending on what type of initial data it refers to.

and rescaled the absolute values of $\mathcal{H}$ as before. The results for both initial data configurations are shown in the plots of Figure 4.2.

For the Gaussian configuration of the fields, we obtain convergence at the expected rate even with a small number of points in the angular directions. This is to be expected since, in this case, both the spacetime and scalar field are spherically symmetric and spatial derivatives in $\theta$ and $\varphi$ vanish identically. However, in the case of the dipolar configuration, one must increase $N_\theta$ and $N_\varphi$ to at least double of the values used in the Gaussian case, as can be read in Table 4.1. For these initial data, the most rapidly varying component in the angular directions is the one proportional to the spherical harmonics $Y_{22} + Y_{2-2} \propto \cos(2\varphi)\sin^2\theta$, therefore requiring a more dense sampling of spacetime to accurately approximate differential operators by finite differences. Nevertheless, for this set of parameters, the rate of convergence of $\mathcal{H}$ to zero is the expected one, especially around the points where the scalar field dominates (around $r/M \approx 5$). In the remaining parts of the domain, the Hamiltonian constraint violation does not converge as expected, hinting at other effects, such as floating point precision, dominating the

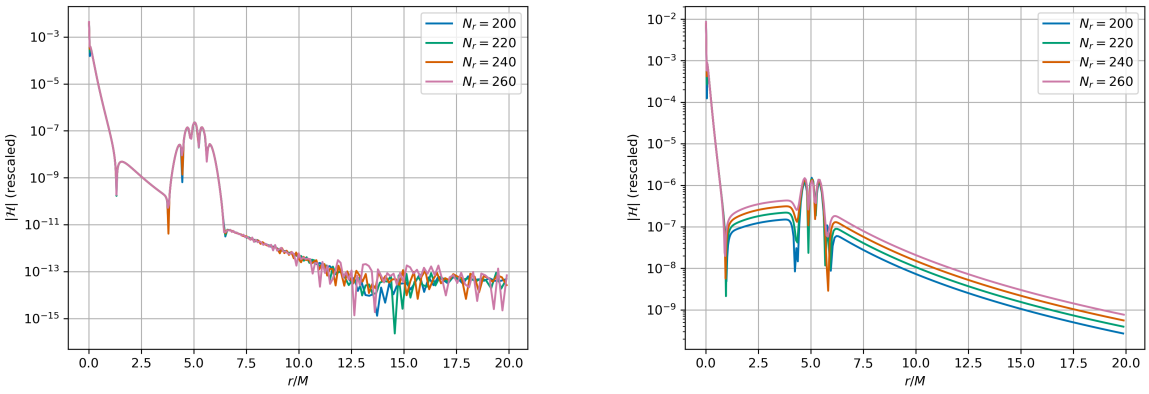


(a) Gaussian initial data

(b) Dipolar initial data

Figure 4.2: Convergence tests for the nonlinear evolution of a scalar field $\Phi$ in a isotopic Schwarzschild spacetime. Both plots correspond to the absolute value of the Hamiltonian constraint violation at the initial time slice $t = 0$. Plot (a) shows the convergence for Gaussian type initial data, whilst plot (b) shows the convergence for dipolar type initial data.

error, instead of the finite difference operators. In fact, if $|\mathcal{H}|$ is not rescaled, the plots in those regions superpose perfectly, giving merit to this idea.

The analysis above shows that the constraint-satisfying initial data expressions were correctly implemented. Furthermore, through analytical manipulation of the expressions in Wolfram Mathematica, we were able to confirm the claims of the reference that indeed these initial data solve the constraints. Therefore, we can confidently use this implementation to probe interesting phenomena that might happen in systems of scalar fields non-linearly coupled to gravity in Schwarzschild black hole spacetimes. We note, however, that while the implementation allows one to use these initial data expressions for the fields in a Kerr background metric, the constraints will be violated in that case. Furthermore, the fact that no correction was applied to the metric quantities – namely the conformal factor – for the pseudo-bound initial data in our implementation means that these too are constraint-violating expressions. Therefore, these cases will be studied from the point of view of what one could expect to see if proper constraint-satisfying initial data were set up, rather than the means for precise simulation of realistic physical scenarios.

## 4.4 Non-linear scattering of massless scalar fields

In this section we aim to explore qualitatively the interaction of massless scalar fields with black hole spacetimes, through numerical evolution. The scalar fields are initialised to the expressions of the previous section and reference [62], describing constraint-satisfying initial data for Schwarzschild backgrounds. Specifically, we shall focus here on the dipolar configurations exclusively. However, we shall also use those same data to explore the evolution on rapidly spinning Kerr geometries. The metric quantities are initially given by the quasi-isotropic expressions of section 4.1 and reference [52] in both spinning and non-spinning cases, since this metric is trivially reduced to Schwarzschild in isotropic coordinates when the dimensionless spin parameter $\chi$ is set to zero.

### 4.4.1 Massless scalar fields in a Schwarzschild background

To set a baseline knowledge of what to expect, we began by evolving a scalar profile with amplitude $A_{11} = 0.04$, centred around $r_0/M = 6.0$ and with width $w = 2.0$. The initial configuration of the spacetime geometry is given by the Schwarzschild metric in isotropic coordinates, with mass $M = 1$. Furthermore, for this evolution the outer boundary of the computational domain was set to $R_{\text{max}} = 100.0$, and the domain was covered by $N_r = 398$ points in the radial direction, distributed according to relation (3.27) and $w_s = 0.25$, as described in sections 3.3.1 and 3.3.2. The values of $N_r$ and $w_s$ were chosen in such a way that the region behind the event horizon was covered with at least 15 points[6], whilst ensuring that the gaussian profile of the scalar field could be resolved throughout the whole computational domain[7]. The

[6] The region inside the horizon is characterised by large values for the derivatives of metric quantities. Therefore, to ensure a good enough approximation with finite difference operators, one must cover this region with a sufficiently large number of points.

[7] From early simulations, we discovered that not being able to resolve the scalar field gaussian throughout the whole domain led to the appearance of spurious oscillations in the scalar field, which quickly propagated to the interior of the domain and spoiled the evolution. Empirically we found that imposing the minimum radial distance between two consecutive grid points to be half of the width $w$ of the gaussian profile allowed for the complete elimination of these oscillations.

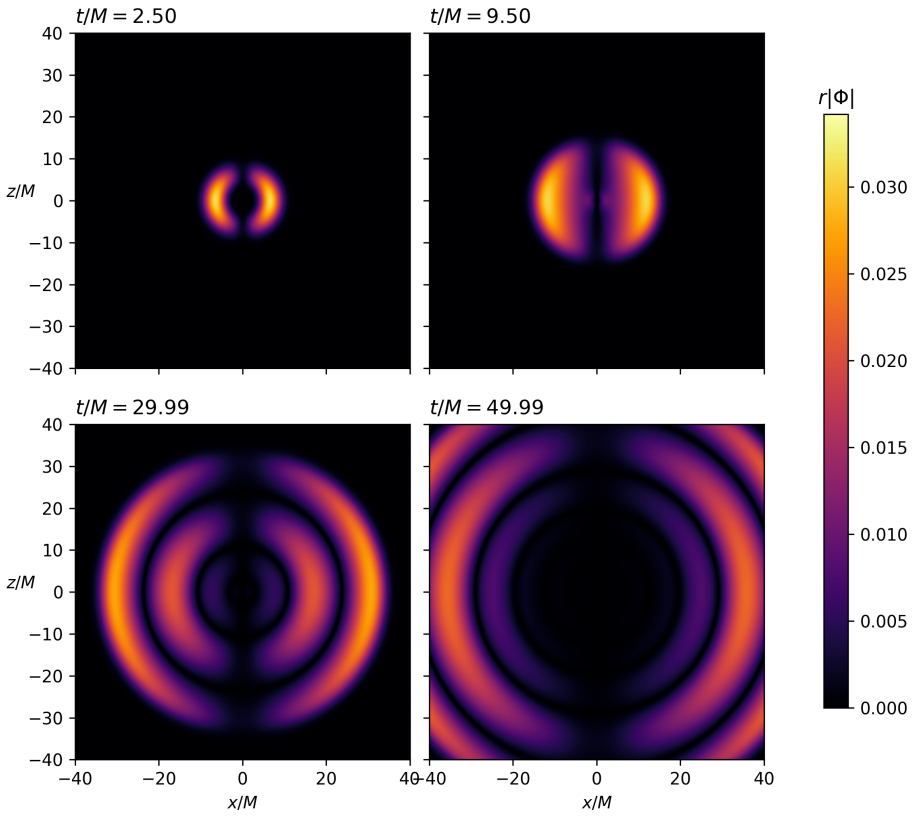


Figure 4.3: Snapshots of the scalar field profile in a Schwarzschild background, for four instants of time. These snapshots were obtained by taking two-dimensional slices of the spatial hypersurfaces of constant coordinate time $t$ along the direction $\varphi = \pm\pi/2$. The $x$ coordinate is redefined accordingly.

number of points in the angular directions correspond to those of Table 4.1 for the dipolar configuration.

In Figure 4.3 we have a visualisation of the scalar field profile for four different values of the coordinate time $t$. Before we analyse these, however, it is important to understand how the plots were obtained. The plots correspond to a two-dimensional slice of the three-dimensional hypersurface $\Sigma_t$ of constant time $t$. Specifically, the slicing contains those grid points with coordinate $\varphi$ closest to $\pm\frac{\pi}{2}$. With this choice, the $x$ coordinate, corresponding to the bottom axis of each plot, was redefined to

$$x = r \sin\theta \cos\left(\varphi + \frac{\pi}{2}\right), \tag{4.40}$$

as opposed to the usual relation (3.26a). The $z$ coordinate is still given by equation (3.26c), since it does not depend on $\varphi$. The time instants that are represented in Figure 4.3 were chosen in a way that would illustrate the main phases of the evolution.

We now look at the plots of Figure 4.3. On the top left plot, corresponding to $t/M = 2.5$, we see a very early configuration[8] of the field. The angular profile is clearly dipolar, whilst in the radial direction the configuration is Gaussian, as expected from the provided initial data. The field is, then, propagated towards the origin and towards spatial infinity until, some time later, it reaches the vicinity of the event

[8]We don't show here the initial configuration of $\Phi$, *i.e.* its configuration at $t = 0$, because, as noted in the discussion of section 4.3, $\Phi$ is initialised to 0, and the non-zero initial data is assigned to $\Pi$ instead. Therefore, we must probe the field at some later instant to get non-zero values.

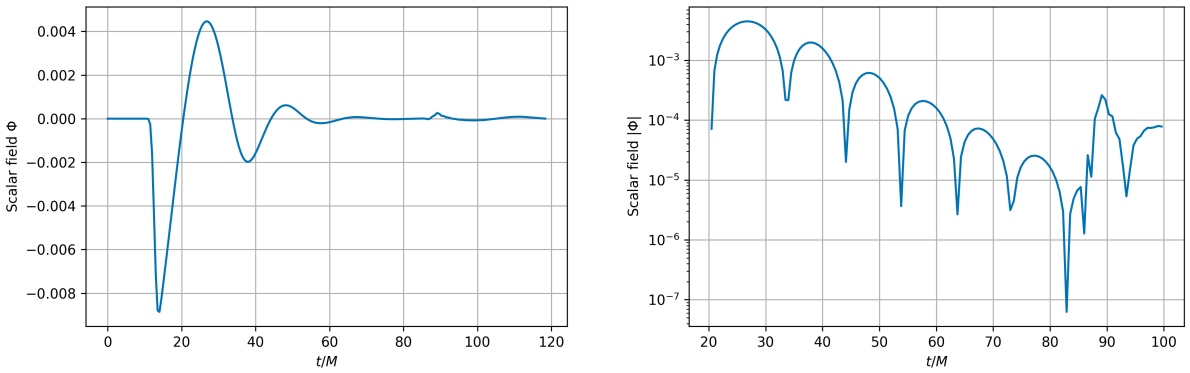


(a) Scalar field at a point

(b) Ringdown phase

Figure 4.4: Sampling of a scalar field $\Phi$ at a single point of the domain, as function of time, for an evolution in an initially Schwarzschild geometry. Plot (a) shows the behaviour of the field at the point with coordinates $r/M \approx 15$, $\theta \approx \pi/2$, $\varphi \approx 0$ for the full simulation time. Plot (b) focuses on the ringdown phase at the same point, displaying the quasi-normal oscillation in the scalar channel.

horizon, located at $r_h/M = \frac{1}{2}$ for this configuration. In the top right panel we can see the first stages of the interaction of the field with the black hole. The interaction is such that new scalar pulses are created, with decreasing amplitude, and propagated to infinity, as can be seen from the two bottom images.

To understand this scattering behaviour, we must introduce the concept of quasi-normal modes of black hole perturbations. In 1973, Saul Teukolsky investigated linear perturbations of Kerr spacetimes [63] (for a recent review, see [64]). The article studies perturbations of spin $\frac{1}{2}$ (Dirac fields), spin 1 (electromagnetic fields) or spin 2 (gravitational fields), but scalar perturbations of spin 0 can be described in the same manner. One of the findings of this work is that all linear perturbations of Kerr obey a single master equation, which can be separated into an ODE for the radial profile and another one for the angular dependence, similarly to what happens with the Schrödinger equation for the hydrogen atom. The angular part can be solved using spin-weighted spheroidal harmonics [65], while the radial equation gives rise to *quasi-normal oscillations*. These are analogous to normal modes in isolated systems, but since the system is dissipative[9], the oscillation frequency $\omega_{\text{QNM}}$ becomes complex, with its imaginary part $\omega_I$ being responsible for a decay in amplitude over time. This is consistent with what is shown in Figure 4.3.

In order to further probe the quasi-normal ringdown of the Schwarzschild spacetime with a scalar non-linear perturbation, we took a narrower initial data profile, namely with width $w = 0.5$, centred around $r_0/M = 5.0$ and of amplitude $A_{11} = 0.075$, and performed a new numerical evolution. A narrower profile, however, means that the radial distribution of grid points must be adjusted, so that our criteria of points inside the event horizon and ability to resolve the gaussian pulse are met. For this simulation we found the best grid parameters to be $N_r = 544$ and $w_s = 0.37$. Furthermore, the boundary was set at $R_{\text{max}} = 50.0$ to keep simulation times manageable. All other parameters keep the values from the previous simulation, including the number of points in the angular directions.

The data from the simulation was then probed at a single point with the intention of identifying the

[9]Energy can escape through the event horizon or towards spatial infinity.

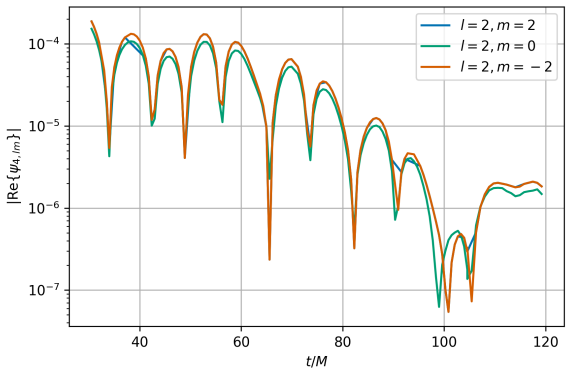


Figure 4.5: Dominant modes of quasi-normal oscillation in the gravitational wave channel, through the Weyl scalar $\Psi_4$, in a Schwarzschild background.

quasi-normal oscillations of the field qualitatively. To that end, in Figure 4.4 we display the profile, over time, of the scalar field at a single point, of coordinates[10] $r/M \approx 15$, $\theta \approx \pi/2$, $\varphi \approx 0$. On the left plot we show the behaviour of the field for the whole simulation time. Several phases can be identified here: at $t = 0$, as expected, we have $\Phi = 0$; after some time, since the sampling radius is greater than $r_0$, the scalar pulse propagating towards infinity passes through the sampling point, and the amplitude starts oscillating; finally, at $t/M \approx 90$ we see a small, but noticeable, perturbation of the signal, due to the propagation of noise from the boundary. Because of the fact that the initial pulse is positioned fairly close to the horizon, where the quasi-normal ringdown originates, it is difficult to clearly separate the quasi-normal oscillation from the propagation of the initial pulse. Nevertheless, on the right plot of Figure 4.4 we see an oscillation pattern of approximately constant frequency and exponential decay, which is consistent (at least from a qualitative standpoint) with perturbation theory and with the results of Okawa *et al.* [62]. Again, at $t/M \approx 90$ we see the effects of the approximate boundary conditions that are propagated towards the interior and dominate over the numerical solution.

With the help of the diagnostic tools implemented within NRPy+, we can also extract the gravitational wave signal that is generated by the scalar perturbation introduced into the Schwarzschild spacetime. To do so, NRPy+ implements a module that generates C code for the computation of the Weyl scalar $\Psi_4$, a quantity featured in the Newman-Penrose formalism [66] that, in broad terms, encodes the outgoing gravitational wave signal. Furthermore, NRPy+ can also generate code for spin-weight -2 spherical harmonics ${}_{-2}Y_{lm}$, which are the eigenfunctions of the angular Teukolsky equation for a Schwarzschild spacetime. We can, then, decompose $\Psi_4$ into its $l, m$ mode by computing the inner product

$$\Psi_{4,lm} = \int_{-\pi}^{\pi} \int_{0}^{\pi} \Psi_4 \left(t, r, \theta, \varphi\right) \, {}_{-2}Y^*_{lm} \left(\theta, \varphi\right) \sin\theta \, \mathrm{d}\theta \, \mathrm{d}\varphi, \tag{4.41}$$

where the integrals are computed numerically using a simple quadrature algorithm.

For the simulation described above, for which the quasi-normal oscillation of the scalar field of Figure 4.4 was observed, we also extracted the gravitational wave signal with the method outlined in the pre-

[10] The coordinates are only given approximately as, since the grid is cell-centred and the radial coordinate is given by expression 3.27 as a function of the computational coordinate $\mathrm{x0}$, points with these exact coordinates may not exist in the grid. Therefore, we search for the point whose coordinates are as close as possible to these reference values.

vious paragraph. The results for the dominant modes are shown in the plot of Figure 4.5. These data, corresponding to an extraction radius of $r/M \approx 30$, show a similar behaviour to what was found in the scalar channel, and consistent with the findings of Okawa *et al.* [62] and black hole perturbation theory. The plots show an oscillation of roughly constant frequency, with exponential decay in amplitude.

With the data presented above for the scalar field at a constant point, as a function of time, an attempt was made to determine the quasi-normal frequencies for the dominant modes of oscillation. This was done by decomposing the scalar signal into spherical harmonics[11], in analogy with equation (4.41), and fitting a exponentially damped sinusoid to the data. The results of this analysis, however, were not satisfactory, revealing a 10% to 20% difference between our results and those predicted in the data files provided in [67], so we chose not to show them. The extraction of black hole mass and spin shown in reference [62] for similar evolutions sheds some light on the effects that may justify this difference. The authors show that the interaction of the scalar cloud with the black hole is responsible for accretion of a relevant portion of the scalar field, leading to increase of black hole mass and spin-up for fields with large enough amplitude. This change of black hole parameters leads to a change in the predicted quasi-normal frequencies and, in fact, the increase in black hole spin of 15% to 20% shown in the reference can account for the increased quasi-normal frequency obtained from our fits. Nevertheless, without accurate measurement of black hole properties, *e.g.* through the deployment of an apparent horizon finder, we can not take this argument with certainty.

### 4.4.2 Massless scalar fields in a Kerr background

We now turn our attention to the evolution of massless scalar fields in Kerr spacetimes, to understand what is the influence of the rotation and lack of spherical symmetry on the evolution. To do so, we set up initial data for the field using the same parameters as in the Schwarzschild case of Figure 4.3, *i.e.* a dipolar profile with amplitude $A_{11} = 0.04$ and Gaussian width $w = 2.0$, centred around $r_0/M = 6.0$. As for the initial spacetime configuration, we kept $M = 1$ and increased the dimensionless spin to $\chi = 0.95$. For this configuration, the required number of points in the radial direction is $N_r = 452$, with $w_s = 0.22$ and $R_{\mathsf{max}}/M = 100.0$. The values for $N_\theta$ and $N_\varphi$ are carried over from the previous simulations.

With the initial data described above, we obtained the plots of Figure 4.6. These were obtained exactly in the same manner as the analogous ones of Figure 4.3 for the spin 0 case. The time slices chosen for these plots are also approximately the same as in the previous case, to allow for a direct comparison between the two. Focusing on the top left plot, and comparing to the Schwarzschild case, there seems to be no discernible difference. This is, of course, justified by the fact that the initial configuration for the scalar field is exactly the same in both cases, and $t/M = 2.50$ is still a very early moment in the evolution, where the effects of the geometry are still insignificant. However, looking at the top right plot, we begin to see evidence of the different spacetime configuration: the distribution of the scalar cloud is not axisymmetric anymore, with the left side of the configuration showing greater absolute values for the field. This asymmetry is caused by the frame-draggin effects of the Kerr spacetime, which force the field

[11] Note that spin-weighted spheroidal harmonics reduce to the usual spherical harmonics when $s = 0$ and $a\omega = 0$, where $a = M\chi$ is the black hole spin.

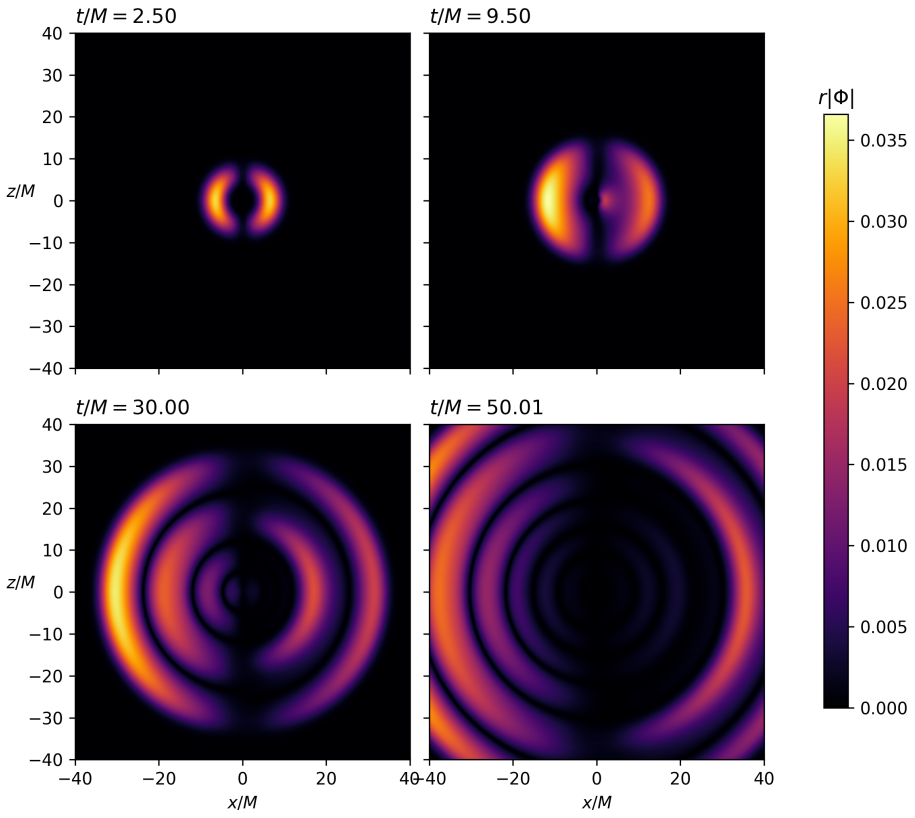


Figure 4.6: Snapshots of the scalar field profile in a Kerr background, for four instants of time. These snapshots were obtained by taking two-dimensional slices of the spatial hypersurfaces of constant coordinate time $t$ along the direction $\varphi = \pm\pi/2$. The $x$ coordinate is redefined accordingly.

to co-rotate with the geometry[12]. However, just like in the non-rotating case, quasi-normal oscillation and ringdown seems present, with the appearance of pulses near the horizon with decreasing amplitude.

To follow the path we took for the evolution of the scalar field in a Schwarzschild spacetime, we performed an evolution of a narrower profile with the intention of studying the quasi-normal oscillatory behaviour in a rotating black hole geometry. The parameters for the field and metric remain unchanged from the non-spinning case, other than the dimensionless spin of the black hole, which is set to $\chi = 0.95$. For this configuration, a computational grid with $N_r = 626$ points in the radial direction was used, with parameters $R_{\text{max}}/M = 50.0$ and $w_s = 0.32$ in order to ensure accurate evolution of the scalar pulse. The number of points in $\theta$ and $\varphi$ were, again, kept constant.

Like in the non-spinning case of section 4.4.1, we sampled the scalar field at a grid point with coordinates $r/M \approx 15$, $\theta \approx \pi/2$, $\varphi \approx 0$. The result is plotted on the left-hand side of Figure 4.7, which is very similar to the corresponding plot in Figure 4.4. As before, the field is zero until the pulse passes through this point, starting at $t/M \approx 17$. Then, the field oscillates with decreasing amplitude, and at $t/M \approx 90$ an effect of the propagation of numerical error from the boundary is visible.

The plot on the right side is focused on the ringdown, and the vertical axis is in logarithmic scale to help visualisation. Comparing with the Schwarzschild case, we can see that, at least on average,

[12]We note here that the $z$ axis, represented in the vertical axis of the plots of Figure 4.6, coincides with the axis of rotation of the Kerr black hole.

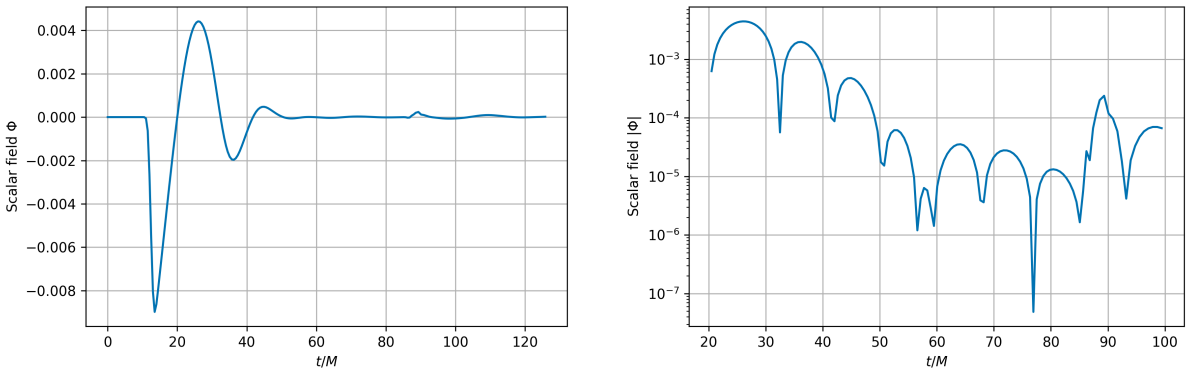


(a) Scalar field at a point

(b) Ringdown phase

Figure 4.7: Sampling of a scalar field $\Phi$ at a single point of the domain, as function of time, for an evolution in an initially Kerr geometry. Plot (a) shows the behaviour of the field at the point with coordinates $r/M \approx 15$, $\theta \approx \pi/2$, $\varphi \approx 0$ for the full simulation time. Plot (b) focuses on the ringdown phase at the same point, displaying the quasi-normal oscillation in the scalar channel.

the oscillation frequency is larger – we see around 8 half-periods of oscillation in this case before the boundary effects dominate, compared to around 6 in the Schwarzschild case. This observation is consistent with perturbative calculations of the frequencies of quasi-normal modes for Kerr black holes: the data files and routines found in [67] (see [64, 68] for details on the calculation of the quasi-normal frequencies) show that $\omega_R$, the real part of the quasi-normal frequency $\omega_{\text{QNM}}$ should increase when the dimensionless spin $\chi$ increases for the dominant $l, m = 1, \pm 1$ modes. However, both $\omega_R$ and $\omega_I$ appear to not be constant over time. Several effects can help explain this behaviour. Firstly, the fact that the initial geometry is that of a rapidly spinning Kerr black hole will promote the excitation of modes with higher $l$, which also decay faster. This leads to a potential mixture of modes at early times. A longer evolution would certainly help in isolating the longer lived fundamental modes. Furthermore, since the evolution is non-linear, *i.e.* the scalar field causes a back-reaction onto the metric quantities, we can expect that the interaction of the scalar cloud with the black hole will lead to accretion of the scalar field, but also extraction of rotational energy from the black hole. Both these effects will change the mass and/or the spin of the geometry and, consequently, the characteristic quasi-normal frequencies. These effects could be explored by using an apparent horizon finder, which would allow for the determination of the mass and spin of the black hole as a function of time. Unfortunately, no such tool was implemented within NRPy+ at the time of writing. However, these effects are explored by Okawa *et al.* [62], and their results give merit to our claims.

We were also able to extract the gravitational wave signal from this simulation, by means of the Weyl scalar $\Psi_4$ and in analogy with what was done for Schwarzschild. The results are shown in Figure 4.8. Direct comparison with the non-spinning case presented in the previous section shows that, in the rapidly spinning case, there is separation in amplitude between the $l, m = 2, 0$ mode and the others with $m \neq 0$, with clear differences in the frequency of oscillation between these modes. However, as before, the behaviour is consistent with the expected quasi-normal ringdown, where the metric oscillates with a definite frequency and approximately exponential decay in amplitude over time.

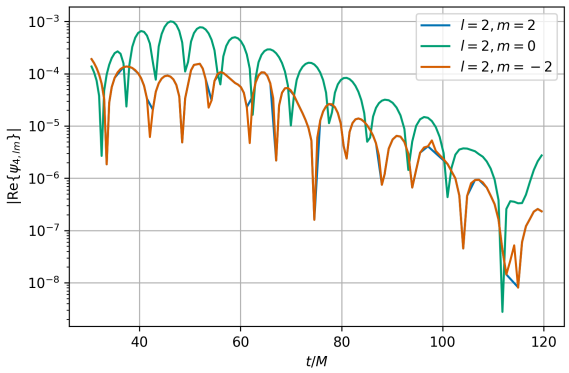


Figure 4.8: Dominant modes of quasi-normal oscillation in the gravitational wave channel, through the Weyl scalar $\Psi_4$, in a Kerr background.

## 4.5 Pseudo-bound states of massive scalar fields

To conclude the analysis of our results, we now focus on an evolution with initial data given by the simplified pseudo-bound states of section 4.3. For this evolution, the scalar field was initialised with an amplitude $A_P = 0.003$, a Gaussian radial profile of width $w = 10.0$ and centred around $r_0/M = 25.0$, with mass term $\mu_S = 0.35$. Furthermore, the frequency and azimuthal number chosen for the pseudo-bound profile were $\omega = 0.3929$ and $m = 1$, respectively. The initial geometry is that of a Kerr black hole with $M = 1$ and $\chi = 0.95$. The value of $\omega$ is one of the values suggested by Okawa *et al.* for the pseudo-bound states, and it should obey condition (1.8) for superradiant amplification, for the chosen values of $m$ and the black hole parameters. The $m$ parameter, an integer, is the smallest non-trivial possible value, since increasing it would necessitate the use of more points in the $\varphi$ direction and slow down the code. The number of points in the radial direction was set to $N_r = 1172$, with $w_s = 0.17$ and $R_{\text{max}}/M = 1000.0$, according to the same criteria used in previous simulations. Given the dependences on the angular coordinates of Equations (4.38) and (4.39), we chose to use $N_\theta = 8$ and $N_\varphi = 16$ as the numbers of points in each angular direction.

One of the objectives of this simulation was to see whether or not long-lived scalar clouds formed around the black hole. Because of that, the boundary was pushed as far away from the origin as possible, whilst keeping a high enough resolution to resolve the fields and the geometry, and an adequate simulation time. With this in mind, we ran the simulation until the coordinate time reached values $t/M \gtrsim 1000.0$. The profile of the fields for six different time instants are shown in the plots of Figure 4.9. These plots differ from those of Figures 4.3 and 4.6, as one might infer from the label of their vertical axis. These correspond to an approximately equatorial slicing of the spatial hypersurfaces[13], *i.e.* across a surface of $\theta \approx \pi/2$. For this type of slicing, there is no need for a redefinition of the Cartesian coordinates.

Going through the plots of Figure 4.9, we start on the top left with the scalar field profile at $t = 0$. As expected, $\Phi \neq 0$ for these initial data. The radial profile is of Gaussian type, while the azimuthal configuration is dipolar due to the $\cos(m\varphi)$ term. The field is then spread out, mostly towards the black

[13]Again, we refer to the slicing as *approximately* equatorial as, since our grid is cell-centred, there is no point matching the condition $\theta = 0$ exactly. The slices, then, correspond to a conic surface of small $\theta$, as close to the equatorial plane $z = 0$ as possible.

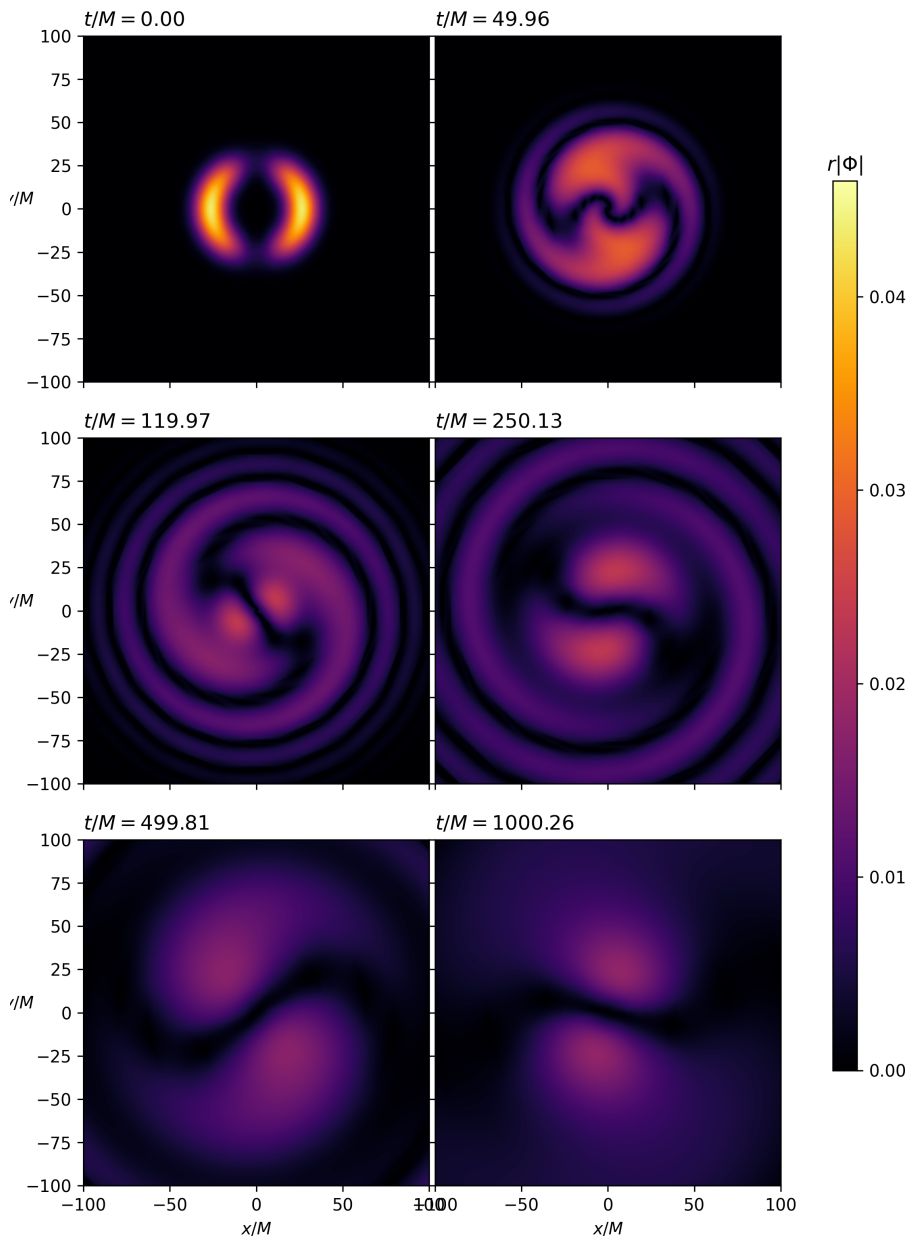


Figure 4.9: Snapshots of the scalar field pseudo-bound state in a Kerr background, for six instants of time. These snapshots were obtained by taking two-dimensional equatorial slices of the spatial hypersurfaces of constant coordinate time $t$.

hole at the origin, and we observe rotation in a counterclockwise direction (in this visualisation). The term $\cos(\omega t + m\varphi)$ in equation (4.38) is responsible for this behaviour. On the two plots in the middle we can see propagation of quasi-normal oscillations towards infinity. This propagation, however, is quite a bit slower than in the massless cases studied in the previous sections. The non-zero mass coupling in this configuration is responsible for the creation of an attractive potential that binds the scalar cloud to the strong field region in the vicinity of the black hole. At $t/M \approx 250$ we can already distinguish the formation of a quasi-bound state, composed by two axially symmetric lobes. The bottom plots show that, whilst these are indeed long lived, being present for the rest of our evolution, they do eventually disperse their energy towards infinity. The results expressed in these plots are consistent with those presented

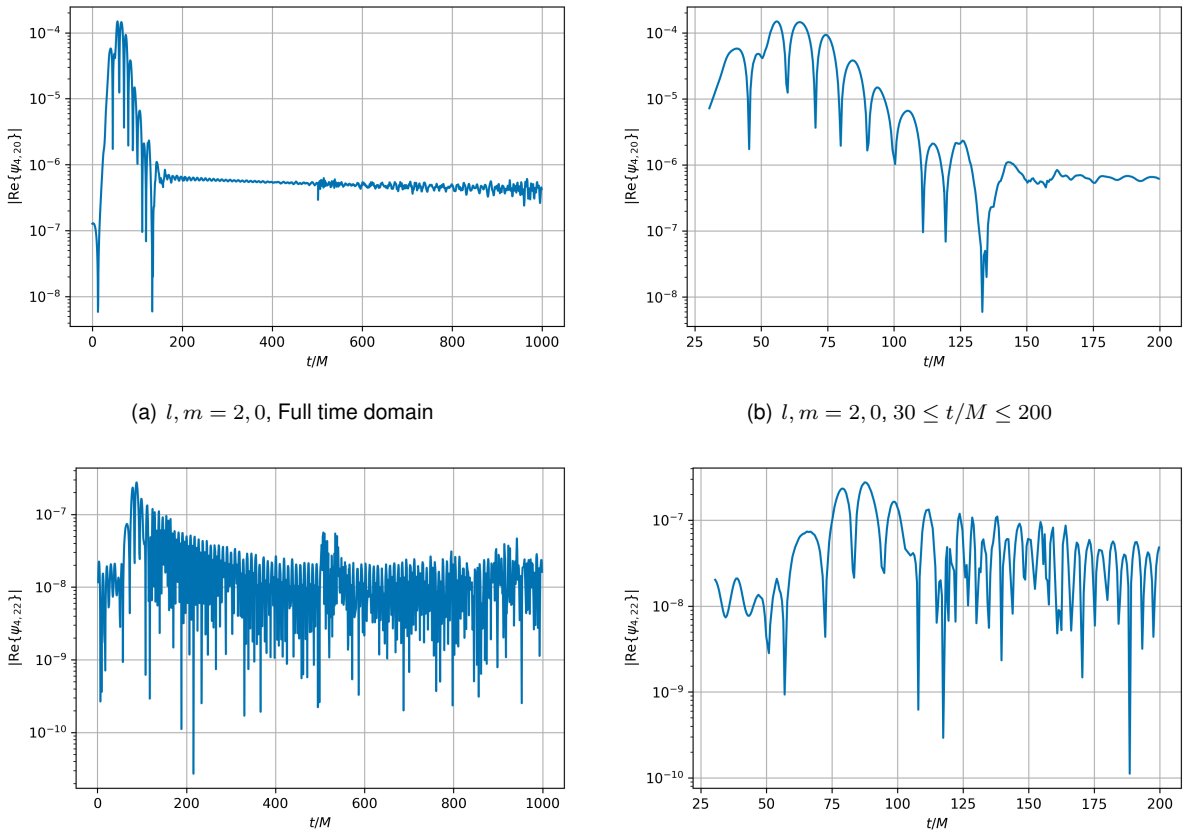


(a) $l, m = 2, 0$, Full time domain

(b) $l, m = 2, 0$, $30 \leq t/M \leq 200$

(c) $l, m = 2, 2$, Full time domain

(d) $l, m = 2, 0$, $30 \leq t/M \leq 200$

Figure 4.10: Results for the extraction of the modes with $l = 2, m = 0, 2$ of the Weyl scalar $\Psi_4$ for a massive scalar field with pseudo-bound type initial data in a rapidly rotating Kerr background. Plots (a) and (c) show each of the modes as a function of time for the full length of the evolution, whilst (b) and (c) focus on the time interval $t/M \in (30, 200)$.

by Okawa *et al.* [62] for their constraint-satisfying pseudo-bound initial data.

As mentioned in the introduction of this dissertation, a particularly compelling reason for studying systems of scalar[14] fields in black hole spacetimes is that these types of fundamental fields are seen as dark matter candidates. Studying their behaviour in strong-field spacetimes and extracting potentially measurable quantities can provide a template for the detection of dark matter from astrophysical sources, much like what has happened with the detection of a gravitational wave signal from a binary black hole merger by the LIGO/Virgo collaboration [15]. With that in mind, we extracted the Weyl scalar $\Psi_4$ at $r/M \approx 30.0$ for this simulation. The results for the modes $l = 2, m = 0, 2$ are displayed in the four plots of Figure 4.10.

The plots on the left of Figure 4.10 show the corresponding modes of $\Psi_4$ as a function of time, for the whole length of the evolution. For the mode $l, m = 2, 0$, a quasi-normal ringdown behaviour is apparent for early coordinate times, consistent with the analysis of previous sections. This is seen more clearly on plot (b), where we focus on the relevant time interval. For the $l, m = 2, 2$ mode, however, this effect is more subtle. By zooming into the same time interval as for the other mode, for $t/M \in (50, 100)$ there seems to be an oscillatory behaviour of more or less constant frequency, even though exponential decay

[14] This argument also applies to vector fields.

is not present. However, beyond the upper limit of the aforementioned time interval, the signal appears more irregular. This could be an effect of the presence of the scalar field itself at the radius of extraction. Since the scalar field in this simulation has a much wider radial profile than in the previous cases, it would have been advantageous to choose an extraction radius that was further away from the origin.

# Chapter 5

# Conclusions

In the previous chapters of this dissertation we have introduced the basic concepts and techniques of Numerical Relativity, such as the 3+1 decomposition of Einstein's equations and the Baumgarte-Shapiro-Shibata-Nakamura formulation; then, we took this knowledge and expanded on it to allow for evolutions in general curvilinear coordinate systems, introducing NRPy+, the numerical tool used for evolutions in this work; finally, we established initial data for both black hole spacetimes and scalar fields in those geometries, and performed evolutions to illustrate the potential results one could draw from our implementation. Now, however, it is time to conclude the work by looking back on everything written in the previous chapters, discussing what was achieved, what could have been improved, and what is left to do.

The list of achievements of this work is extensive, but it may be difficult to grasp for individuals not familiar with the sort of numerical implementation work we presented. Numerical Relativity is, itself, a highly non-trivial subject, for reasons that have been highlighted various times throughout this text, such as the explicit covariance of Einstein's field equations, the ill-posedness of the evolution equations for 3+1 metric quantities, and many others. Furthermore, performing evolutions on curvilinear coordinate systems poses additional problems, which were discussed in detail in Chapter 3, that need to be understood in detail in order to be able to implement code that performs these evolutions. All of that was done in this thesis: we present a rather short, but detailed, description of the topics at hand, making the reader familiar enough with the subject that they can understand the challenges of implementation.

Perhaps the biggest achievement discussed here was the successful implementation, within NRPy+, of the possibility of evolving a real scalar field coupled to the pre-existing interface for evolution of the geometric quantities describing spacetime. This is shown extensively in the results presented in Chapter 4, where we looked at evolutions of scalar fields in black hole spacetimes (both rotating and not), discussed the quasi-normal ringdown in the scalar and gravitational wave channels and showed the existence of long-lived massive scalar clouds in these spacetimes. NRPy+, as most Numerical Relativity codes, is complex, due to the complexity of the subject itself, and the implementation was riddled with many challenges. However, those challenges were addressed, and in the end we were left with a very satisfactory implementation and a substantial amount of results.

However, this work has several shortcomings, most of which justified by the time constraints that a dissertation of this kind is subject to. The most prominent of shortcomings is the lack of precision measurement of various quantities, such as the quasi-normal frequencies and evolution of black hole parameters in time. As mentioned above, the implementation of the evolution equations for the field and inclusion of the correct source terms in the BSSN equations posed many difficulties and, by the time these were taken care of, there was little time to explore the parameter space in a more complete way, as well as to perform very precise evolutions with the parameters we chose. This was unaided by the fact that the code lacks optimisation for running in higher core-count environments, such as computing clusters, which could have made performance better. For these reasons, we chose to focus our efforts in a qualitative showing of the possibilities opened up by the implementation, rather than on precision.

To add to the aforementioned shortcoming, there is a lot of work left for the future. To name a few things that would be interesting to implement and explore, we highlight the expansion of the code to the evolution of complex fields, the implementation of proper constraint-satisfying initial data for scalar fields in Kerr geometries and in pseudo-bound states, further optimisation of the code to take advantage of a wider variety of computing devices, exploration of superradiant effects for very long evolutions and a similar implementation for vector fields and other types of perturbations. This would allow a more accurate comparison between our implementation and the existing results in the literature, and the possibility to take advantage of the characteristics of the code, such as the use of coordinates adapted to the geometry of the problem in study, to provide insight on yet unexplored effects. From the point of view of physics and our understanding of the universe, such studies would allow for the prediction of measurable signals from dark matter candidates and beyond Standard Model physics.

In conclusion, this work as achieved a very satisfactory, albeit incomplete, implementation allowing the fully non-linear evolution of scalar fields in black hole geometries, and has presented results showing the potential for extraction of measurable quantities from these simulations. The work is, however, left unfinished due to time constraints, and should be regarded as a beginning, not a closed system. The way to improve and evolve this work is outlined above, but the results shown are promising.

# Bibliography


[1] A. Einstein. Zur Elektrodynamik bewegter Körper. *Ann. Phys.*, 322(10):891–921, 1905. doi: 10.1002/andp.19053221004.

[2] Karl Schwarzschild. Über das Gravitationsfeld eines Massenpunktes nach der Einsteinschen Theorie. *Sitzungsber. Preuss. Akad. Wiss. Berlin*, pages 189–196, 1916.

[3] C. W. Misner, K. S. Thorne, and J. A. Wheeler. *Gravitation*. Princeton University Press, 2017.

[4] M. D. Kruskal. Maximal extension of Schwarzschild metric. *Phys. Rev.*, 119(5):1743–1745, 1960. doi: 10.1103/PhysRev.119.1743.

[5] G. Szekeres. On the singularities of a Riemannian manifold. *Publ. Mat. debrecen*, 7:285–301, 1960.

[6] H. Reissner. Über die Eigengravitation des elektrischen Feldes nach der Einsteinschen Theorie. *Ann. Phys.*, 355(9):106–120, 1916. doi: 10.1002/andp.19163550905.

[7] G. Nordström. On the energy of the gravitational field in Einstein's theory. In *Verhandl. Koninkl. Ned. Akad. Wetenschap., Afdel. Natuurk., Amsterdam*, number 26, page 1201–1208, 1918.

[8] R. P. Kerr. Gravitational field of a spinning mass as an example of algebraically special metrics. *Phys. Rev. Lett.*, 11(5):237–238, 1963. doi: 10.1103/PhysRevLett.11.237.

[9] B. Carter. Axisymmetric black hole has only two degrees of freedom. *Phys. Rev. Lett.*, 26(6): 331–333, 1971. doi: 10.1103/PhysRevLett.26.331.

[10] S. W. Hawking. Gravitational radiation from colliding black holes. *Phys. Rev. Lett.*, 26(21):1344–1346, 1971. doi: 10.1103/PhysRevLett.26.1344.

[11] S. W. Hawking. Black holes in general relativity. *Commun. Math. Phys.*, 25(2):152–166, 1972. doi: 10.1007/BF01877517.

[12] W. Israel. Event horizons in static vacuum space-times. *Phys. Rev.*, 164(5):1776–1779, 1967. doi: 10.1103/PhysRev.164.1776.

[13] W. Israel. Event horizons in static electrovac space-times. *Commun. Math. Phys.*, 8(3):245–260, 1968. doi: 10.1007/BF01645859.

[14] F. W. Dyson, A. S. Eddington, and C. Davidson. IX. A determination of the deflection of light by the sun's gravitational field, from observations made at the total eclipse of May 29, 1919. *Phil. Trans. R. Soc. A*, 220(571-581):291–333, 1920. doi: 10.1098/rsta.1920.0009.

[15] B. P. Abbott *et al.* (LIGO Scientific Collaboration & Virgo Collaboration). Observation of gravitational waves from a binary black hole merger. *Phys. Rev. Lett.*, 116(6):061102, 2016. doi: 10.1103/PhysRevLett.116.061102.

[16] The Event Horizon Telescope Collaboration *et al.* First M87 Event Horizon Telescope results. I. The shadow of the supermassive black hole. *Astrophys. J. Lett.*, 875(1):L1, 2019. doi: 10.3847/2041-8213/ab0ec7.

[17] R. Brito, V. Cardoso, and P. Pani. *Superradiance*, volume 971 of *Lecture Notes in Physics*. Springer International Publishing, 2nd edition, 2020. doi: 10.1007/978-3-030-46622-0.

[18] O. Klein. Die Reflexion von Elektronen an einem Potentialsprung nach der relativistischen Dynamik von Dirac. *Z. Physik*, 53:157–165, 1929. doi: 10.1007/BF01339716.

[19] Hund. F. Materieerzeugung im anschaulichen und im gequantelten Wellenbild der Materie. *Z. Physik*, 117:1–17, 1941. doi: 10.1007/BF01337403.

[20] Y. B. Zel'dovich. Amplification of cylindrical electromagnetic waves reflected from a rotating body. *Zh. Eksp. Tear. Fiz.*, 62(6):2076–2081, 1972.

[21] J. Maldacena. The large-N limit of superconformal field theories and supergravity. *Int. J. Theor. Phys.*, 38:1113–1133, 1999. doi: 10.1023/A:1026654312961.

[22] S. S. Gubser, I. R. Klebanov, and A. M. Polyakov. Gauge theory correlators from non-critical string theory. *Phys. Lett. B*, 428(1-2):105–114, 1998. doi: 10.1016/S0370-2693(98)00377-3.

[23] W. Edward. Anti-de Sitter space and holography. *Adv. Theor. Math. Phys.*, 2:253–291, 1998.

[24] S. G. Hahn and R. W. Lindquist. The two-body problem in geometrodynamics. *Ann. Phys. (N. Y.)*, 2(2):304–331, 1964. doi: 10.1016/0003-4916(64)90223-4.

[25] L. Smarr. Space-times generated by computers: Black holes with gravitational radiation*. *Ann. N. Y. Acad. Sci.*, 302(1):569–604, 1977. doi: 10.1111/j.1749-6632.1977.tb37076.x.

[26] K. Eppley. Evolution of time-symmetric gravitational waves: Initial data and apparent horizons. *Phys. Rev. D*, 16:1609–1614, 1977. doi: 10.1103/PhysRevD.16.1609.

[27] E. Gourgoulhon. *3+1 Formalism in General Relativity: Bases of Numerical Relativity*, volume 846 of *Lecture Notes in Physics*. Springer-Verlag Berlin Heidelberg, 1st edition, 2012. doi: 0.1007/978-3-642-24525-1.

[28] M. Alcubierre. *Introduction to 3+1 numerical relativity*. Oxford University Press, 2008.

[29] T. W. Baumgarte and S. L. Shapiro. *Numerical Relativity: Solving Einstein's Equations on the Computer*. Cambridge University Press, 2010. doi: 10.1017/CBO9781139193344.

[30] J. Winicour. Characteristic evolution and matching. *Living Rev. Relativ.*, 15(1):2, 2012. doi: 10.12942/lrr-2012-2.

[31] H. Friedrich. Conformal Einstein evolution. In J. Frauendiener and H. Friedrich, editors, *The Conformal Structure of Space-Time: Geometry, Analysis, Numerics*, pages 1–50. Springer Berlin Heidelberg, 2002. doi: 10.1007/3-540-45818-2_1.

[32] F. Pretorius. Numerical relativity using a generalized harmonic decomposition. *Classical and Quantum Gravity*, 22(2):425–451, 2005. doi: 10.1088/0264-9381/22/2/014.

[33] S. R. Brandt *et al.* The Einstein Toolkit, May 2020. URL `https://doi.org/10.5281/zenodo.3866075`.

[34] I. Ruchlin, Z. B. Etienne, and T. W. Baumgarte. $\mathrm{SENR/NRPy+}$: Numerical relativity in singular curvilinear coordinate systems. *Phys. Rev. D*, 97:064036, 2018. doi: 10.1103/PhysRevD.97.064036.

[35] G. Darmois. *Les équations de la gravitation einsteinienne*. Number 25 in Mémorial des sciences mathématiques. Gauthier-Villars, 1927.

[36] A. Lichnerowicz. *Sur certains problèmes globaux relatifs au système des équations d'Einstein*. PhD thesis, Faculté des Sciences de L'Université de Paris, 1939.

[37] A. Lichnerowicz. L'intégration des équations de la gravitation relativiste et le probleme des n corps. *J. Math. Pures Appl*, 23(37):4, 1944.

[38] A. Lichnerowicz. Sur les équations relativistes de la gravitation. *Bull. de la Soc. Math. de France*, 80:237–251, 1952. doi: 10.24033/bsmf.1433.

[39] Y. Fourès-Bruhat. Théorème d'existence pour certains systèmes d'équations aux dérivées partielles non linéaires. *Acta Math.*, 88(1):141–225, 1952.

[40] Y. Fourès-Bruhat. Sur l'intégration des Équations de la relativité générale. *Arch Ration Mech Anal*, 5(6):951–966, 1956.

[41] R. Arnowitt, S. Deser, and C. W. Misner. Republication of: The dynamics of general relativity. *Gen Relativ Gravitn*, 40(9):1997–2027, 2008. doi: 10.1007/s10714-008-0661-1.

[42] J. W. York. Kinematics and dynamics of general relativity. In L.L. Smarr, editor, *Sources of gravitational radiation*, pages 83–126. Cambridge University Press, 1979.

[43] M. Shibata and T. Nakamura. Evolution of three-dimensional gravitational waves: Harmonic slicing case. *Phys. Rev. D*, 52:5428–5444, 1995. doi: 10.1103/PhysRevD.52.5428.

[44] T. W. Baumgarte and S. L. Shapiro. Numerical integration of Einstein's field equations. *Phys. Rev. D*, 59:024007, 1998. doi: 10.1103/PhysRevD.59.024007.

[45] T. W. Baumgarte, P. J. Montero, I. Cordero-Carrión, and E. Müller. Numerical relativity in spherical polar coordinates: Evolution calculations with the BSSN formulation. *Phys. Rev. D*, 87:044026, 2013. doi: 10.1103/PhysRevD.87.044026.

[46] M. Alcubierre, B. Brügmann, P. Diener, M. Koppitz, D. Pollney, E. Seidel, and R. Takahashi. Gauge conditions for long-term numerical black hole evolutions without excision. *Phys. Rev. D*, 67:084023, 2003. doi: 10.1103/PhysRevD.67.084023.

[47] J. R. van Meter, J. G. Baker, M. Koppitz, and D.-I. Choi. How to move a black hole without excision: Gauge conditions for the numerical evolution of a moving puncture. *Phys. Rev. D*, 73:124011, 2006. doi: 10.1103/PhysRevD.73.124011.

[48] J. D. Brown. Covariant formulations of Baumgarte, Shapiro, Shibata, and Nakamura and the standard gauge. *Phys. Rev. D*, 79:104029, 2009. doi: 10.1103/PhysRevD.79.104029.

[49] I. Cordero-Carrión and P. Cerdá-Durán. Partially Implicit Runge-Kutta methods for wave-like equations. In F. Casas and V. Martínez, editors, *Advances in Differential Equations and Applications*, volume 4, pages 267–278. Springer, Cham, 2014.

[50] L. Dagum and R. Menon. Openmp: an industry standard api for shared-memory programming. *IEEE Comput. Sci. Eng*, 5(1):46–55, 1998.

[51] K. A. Dennison and T. W. Baumgarte. A simple family of analytical trumpet slices of the Schwarzschild spacetime. *Class Quantum Gravity*, 31(11):117001, 2014. doi: 10.1088/0264-9381/31/11/117001.

[52] Y. T. Liu, Z. B. Etienne, and S. L. Shapiro. Evolution of near-extremal-spin black holes using the moving puncture technique. *Phys. Rev. D*, 80:121503, 2009. doi: 10.1103/PhysRevD.80.121503.

[53] D. R. Brill and R. W. Lindquist. Interaction energy in geometrostatics. *Phys. Rev.*, 131:471–476, 1963. doi: 10.1103/PhysRev.131.471.

[54] R. C. Tolman. *Relativity, Thermodynamics and Cosmology*. Oxford Press, 1934.

[55] J. R. Oppenheimer and G. M. Volkoff. On massive neutron cores. *Phys. Rev.*, 55:374–381, 1939. doi: 10.1103/PhysRev.55.374.

[56] J. Thornburg. Coordinates and boundary conditions for the general relativistic initial data problem. *Class. Quantum Gravity*, 4(5):1119–1131, sep 1987. doi: 10.1088/0264-9381/4/5/013.

[57] S. Brandt and B. Brügmann. A simple construction of initial data for multiple black holes. *Phys. Rev. Lett.*, 78:3606–3609, 1997. doi: 10.1103/PhysRevLett.78.3606.

[58] J. G. Baker, J. Centrella, D.-I. Choi, M. Koppitz, and J. van Meter. Gravitational-wave extraction from an inspiraling configuration of merging black holes. *Phys. Rev. Lett.*, 96:111102, 2006. doi: 10.1103/PhysRevLett.96.111102.

[59] M. Campanelli, C. O. Lousto, P. Marronetti, and Y. Zlochower. Accurate evolutions of orbiting black-hole binaries without excision. *Phys. Rev. Lett.*, 96:111101, 2006. doi: 10.1103/PhysRevLett.96.111101.

[60] S. Dain, C. O. Lousto, and Y. Zlochower. Extra-large remnant recoil velocities and spins from near-extremal-Bowen-York-spin black-hole binaries. *Phys. Rev. D*, 78:024039, 2008. doi: 10.1103/PhysRevD.78.024039.

[61] S. R. Brandt and E. Seidel. Evolution of distorted rotating black holes. III. initial data. *Phys. Rev. D*, 54:1403–1416, 1996. doi: 10.1103/PhysRevD.54.1403.

[62] H. Okawa, H. Witek, and V. Cardoso. Black holes and fundamental fields in numerical relativity: Initial data construction and evolution of bound states. *Phys. Rev. D*, 89:104032, 2014. doi: 10.1103/PhysRevD.89.104032.

[63] S. A. Teukolsky. Perturbations of a Rotating Black Hole. I. Fundamental Equations for Gravitational, Electromagnetic, and Neutrino-Field Perturbations. *Astrophys. J.*, 185:635–648, 1973. doi: 10.1086/152444.

[64] E. Berti, V. Cardoso, and A. O. Starinets. Quasinormal modes of black holes and black branes. *Class. Quantum Gravity*, 26(16):163001, 2009. doi: 10.1088/0264-9381/26/16/163001.

[65] E. Berti, V. Cardoso, and M. Casals. Eigenvalues and eigenfunctions of spin-weighted spheroidal harmonics in four and higher dimensions. *Phys. Rev. D*, 73:024013, 2006. doi: 10.1103/PhysRevD.73.024013.

[66] E. Newman and R. Penrose. An approach to gravitational radiation by a method of spin coefficients. *J. Math. Phys.*, 3(3):566–578, 1962. doi: 10.1063/1.1724257.

[67] V. Cardoso. Ringdown data and routines. URL `https://centra.tecnico.ulisboa.pt/network/grit/files/ringdown/`. (accessed: 21/12/2020).

[68] E. Berti, V. Cardoso, and C. M. Will. Gravitational-wave spectroscopy of massive black holes with the space interferometer LISA. *Phys. Rev. D*, 73:064030, 2006. doi: 10.1103/PhysRevD.73.064030.